LATVIAN JOURNAL of PHYSICS and TECHNICAL SCIENCES

ISSN 0868 - 8257

2

Institue of Physical Energetics-70

(Vol. 53)

2016

Ind. pasūt. € 1,50 Indekss 2091
Org. € 15,00 Indekss 2092

SATURS

ENERĢĒTIKAS FIZIKĀLĀS UN TEHNISKĀS PROBLĒMAS

CIETVIELU FIZIKA

LIETIŠĶĀ FIZIKA

RADIOASTRONOMIJA

Price to individual subscribers € 1.50/issue Index 2091
Price to collective subscribers € 15.00/issue Index 2092

CONTENTS

Индивид. заказ. Є 1,50 Индекс 2091
Орг. заказ. Є 15,00 Индекс 2092

СОДЕРЖАНИЕ

LATVIAN JOURNAL of PHYSICS and TECHNICAL SCIENCES

LATVIJAS FIZIKAS un TEHNISKO ZINĀTŅU ŽURNĀLS

ЛАТВИЙСКИЙ ФИЗИКО-ТЕХНИЧЕСКИЙ ЖУРНАЛ

Published six times a year since February 1964
Iznāk sešas reizes gadā kopš 1964. gada februāra
Выходит шесть раз в год с февраля 1964 года

2 (Vol. 53) • 2016

RĪGA

INDEKSĒTS (PUBLICĒTS) | INDEXED (PUBLISHED) IN

www.scopus.com
www.degruyter.com
Emerging Sources Citation Index (ESCI),
EBSCO (Academic Search Complete, www.epnet.com), INSPEC (www.iee.org.com).
VINITI (www.viniti.ru), Begell House Inc/ (EDC, www.edata-center.com).

Izdevējs: Fizikālās enerģētikas institūts
Reģistrācijas apliecība Nr. 0221
Redakcija: Aizkraukles ielā 21, Rīga, LV-1006
Tel. 67551732, 67558694
e-pasts: ezerniec@edi.lv
Interneta adrese: www.fei-web.lv
Iespiests SIA “AstroPrint”

LATVIAN JOURNAL OF PHYSICS AND TECHNICAL SCIENCES
2016, N 2

DOI: 10.1515/lpts-2016-0008

PHYSICAL AND TECHNICAL ENERGY PROBLEMS

SHORT-TERM FORECASTING OF LOADS AND WIND POWER FOR LATVIAN POWER SYSTEM: ACCURACY AND CAPACITY OF THE DEVELOPED TOOLS

V. Radziukynas, A. Klementavičius

Riga Technical University,
1 Kalku Str., Riga LV-1658, LATVIA

The paper analyses the performance results of the recently developed short-term forecasting suit for the Latvian power system. The system load and wind power are forecasted using ANN and ARIMA models, respectively, and the forecasting accuracy is evaluated in terms of errors, mean absolute errors and mean absolute percentage errors. The investigation of influence of additional input variables on load forecasting errors is performed. The interplay of hourly loads and wind power forecasting errors is also evaluated for the Latvian power system with historical loads (the year 2011) and planned wind power capacities (the year 2023).

Keywords: *forecasting error, short-term forecasting, system load, wind power, wind speed.*

1. INTRODUCTION

The ongoing large-scale integration of wind power plants into EU countries and extended cross-border transfers of load flows bring challenges to transmission system operators (TSOs) as how to schedule and control the intermittent loads, generation and transit in a transparent, secure and optimal way [1]–[3]. It leads to the increased need for short-term forecasts enabling TSOs to better match generation and loads and reduce the transboundary propagation of related imbalances [1]–[3].

The need for a good short-term forecasting practice is arising in Latvia as well where (1) the adequacy of system loads and generation is highly dependent on availability of hydro resources; (2) the high transit across Baltic power system (PS) are expected with implementation of the Baltic Energy Market Interconnection Plan (BEMIP); and (3) large wind power capacities (in respect of system load) will be connected to: up to 500 MW in Latvian PS by 2023 and 800 MW and 1000 MW in neighbouring Lithuanian and Estonian PSs, respectively [4]–[6].

In response to the situation as such, a new short-term forecasting suit was

developed consisting of 3 tools (computer programs). *LOADS-LV* and *WIND-LV* tools serve for system load and wind power forecasting, respectively, and are based on the well-known forecasting models: ANN (Artificial Neural Network) – for loads and ARIMA (Autoregressive Integrated Moving Average) – for wind power. *JOINT-LV*, the 3rd tool, serves for the combined forecast. In general, both ANN and ARIMA models are problem dependent and their customisation to the problem is often conditioned on input data. The tools are customised to Latvian weather and load profile situation. The current paper aims at the evaluation of operability and effectiveness of these tools.

The early application of ANN model for short-term load forecasting refers to 1992 [7] and first comprehensive review of models application seems to be published in 2001 [8]. Although a number of authors point to the good forecasting results, it can hardly be generalised as a rule. Specifically, when dealing with the complete set of all the days in the year, which present dissimilar profiles, the ANN model cannot offer good forecasts [9].

The forecasting for wind power gained momentum in the early 1990s when the increase of the installed wind energy capacity all over the world attracted the attention of electricity companies, wind energy promoters and researchers towards the short-term prediction, mainly motivated by the necessity of integration into the grid of an increasing "unknown" (fluctuating) amount of wind power. The comprehensive review of the forecasting methods over the 30-year period can be found in [10]. ARIMA and other time series models were addressed to significant extent and some authors point to a good performance of ARIMA model [11], [12]. Nevertheless, since acceptable forecasting time horizon of ARIMA is 6–10 h, the strengthening of ARIMA capacity is achieved by means of its modification, e.g. fractional-ARIMA [13] or hybrid applications (combined with other models) [14], [15].

In addition to the evaluation of performance of the developed forecasting tools, the current paper sets the goals to investigate:

1) How influential may additional input variables (weather temperature, wind speed, weekday index) be on the accuracy of load forecasting?

2) Presuming that forecasting errors of load and wind power should be compensated by Latvian TSO, what decrease of load-frequency regulation reserves could be gained due to the self-cancellation of positive and negative errors?

2. INPUT TO FORECASTING TOOLS

The following input variables have been applied to the forecasting models:

- *for load forecasting (LOADS-LV* tool*):*

(1) Historical power system loads [16];

(2) Weekday index (workday, weekend) of a load;

(3) Past and future (next-day) weather temperatures (both historical);

(4) Past and future (next-day) wind speeds at 10-m height (both historical);

- *for wind speed forecasting (WIND-LV* tool*):*

(5) Historical wind speeds at 10-m height.

All variables are presented as hourly data. The data arrays elapse over 4 months, from 1 Nov 2011 to 29 Feb 2012, which constitute an investigation period. Data (3)–(5) are records of meteorological data for Riga site (Central Latvia) [17]. They can be *a priori* thought of as all-Latvian averages.

The input data (1)–(4) are employed for model identification, training, validation, testing and forecasting purposes, while the input data (5) – for model identification and forecasting purposes.

Since Ref. [17] presents the wind speeds as whole numbers (e.g. 5 m/s), these should be considered very rough values for forecasting purposes. We derived the "rounded out" values from these whole numbers by adding a random fraction (-0.4, -0.3,…,0.5). Thus, the "rounded out" speeds contain one decimal number after the decimal point (e.g. 5.4 m/s).

The load profile over the investigation period seems to be rather variable with mean load 890 MW, maximum load 1320 MW and, respectively, the load factor 0.67. Separated by weekday type, mean workday load accounts for 925 MW vs mean weekend load 815 MW. The minimum load in the investigation period is recorded 510 MW. The temperatures range from -30 °C to 10 °C. The maximum hourly wind speed (10-m height) was 11 m/s and the number of calm hours (at a wind speed < 2m/s) was 255 h from a total of 2904 h.

The wind power capacity was simulated to be connected in amount of 500 MW.

3. FORECASTING PROCEDURE

3.1. Load Forecasting Procedure

As known, ANNs are trained by adapting a network and comparing the output obtained with the input training and target data. The training is carried out until the network output matches the target data. Feed forward neural networks permit the signals to travel from an input layer to an output layer in only one way, which means that the output of any layer does not affect the same layer. The layer in between these two layers is the hidden layer. The neural networks use weights for each input variable and a bias that acts as a threshold to produce outputs. They further use learning algorithms to fine tune the weights and biases of a network such that the output can be obtained from the weights and biases. The learning algorithm is effective if a small change in the weights and biases leads to a small change in the output [18].

The load forecasting was performed in the sequence of steps corresponding to algorithms implemented in the *LOADS-LV* tool.

1) *Network Identifier*

The algorithm works within the MATLAB toolbox ANN. It sets up (identifies) the structure and characteristics of the neural network so as to fit a specific problem. Like in usual practices, a network is identified by experimentation. Identification period for the considered problem was chosen 3 months back from the start of the forecasting period (1 Feb 2012). Four network models were identified (and subsequently trained, see an algorithm below) using 4 different identification data sets (Table 1):

Table 1

Identification Results of ANN for Latvian Short-term Load Forecasts

Identification characteristic	Identification data set			
	workday loads only	weekend loads only	workday loads, temperatures, wind speeds	weekend loads, temperatures, wind speeds
Network type/paradigm	feed forward	feed forward	feed forward	feed forward
Number of hidden layers	2	2	2	2
Number of hidden neurons	1st layer – 3 2nd – 4	1st layer – 6 2nd – 4	1st layer – 6 2nd – 7	1st layer – 7 2nd – 7
Transfer function	linear	linear	linear	Linear

2) *Network Trainer/ Retrainer*

This algorithm works mostly concurrently with *Network Identifier*. It trains the identified network to find the implicit relations between the input variables and outputs. The outputs are next day hourly loads (forecasts). The training period coincides with the identification period (1 Nov 2011 – 31 Jan 2012) and is split to 70 % of hours for training, 15 % for validation and 15 % for testing. The supervised training was exercised when the weekday index was pointed to.

The separate training sets were applied for workdays and weekend days as well as for baseline input (loads) and extended input (loads, temperatures, wind speeds).

3) *Load Forecaster*

This algorithm produces 24-hour load forecasts for the next day imitating the forecasting time at 24:00 of the previous day and using the input of historical data from the 3 preceding months. The input period is moved consecutively by one day for each new day. In the end, the last new day of the forecasting period was 29 Feb, with the preceding input period from 29 Nov to 28 Feb. During the process, the retraining was not addressed.

4) *Accuracy Evaluator*: Load power forecasts are compared with actual wind powers and the relevant forecasting errors are calculated: errors, absolute errors (AE), mean absolute errors (MAE), absolute percentage errors (APE), mean absolute percentage errors (MAPE), etc.

3.2. Wind Power Forecasting Procedure

The indirect forecasting of wind power is implemented by the forecasting tool *WIND-LV*, i.e. wind power forecasts are not derived from historical wind power time series but calculated from the wind speed forecasts.

The ARIMA model was taken as a basis for *WIND-LV* as most promising for purpose of this investigation after preliminary revision of parametric models ARMA, ARX, ARMAX, ARIMAX, etc. The ARIMA model is expressed as follows:

$$A(q)y(t) = \frac{C(q)}{(1-q^{-1})}e(t), \tag{1}$$

where $y(t)$ – direct system output at time moment t;
q – time delay operator, i.e. $q^{-1}u(t)=u(t-1)$;
$u(t-1)$ – input signal;
A, C – polynomials;
$e(t)$ – white noise.

WIND-LV consists of the following algorithms:

1) *Height Calculator*: Time series of historical wind speeds at 10-m height is upscaled to the time series for the selected hub heights. For the problem in question, the "rounded-out" wind speeds were converted to those at 80-m height using classical Hellman exponential law formula [19]:

$$\frac{v}{v_0}=\left(\frac{H}{H_0}\right)^{\alpha}, \tag{2}$$

where v – speed to the height H;
v_0 – speed to the height H_0;
α – friction coefficient or Hellman exponent. Assuming that the Latvian wind farms would be constructed in open landscape, α value was taken to be 0.14 [19].

2) *ARIMA Identificator*: Structure of ARIMA model is identified using MATLAB ARIMA toolbox.

In the considered problem, Latvian wind speed data of Jan 2012 were used for model identification. The procedure was done by experimentation in the same way as in [20]. Identification resulted in parameter values p=3, d=1 and q=4.

3) *Speed Forecaster*: The ARIMA model produces the short-term forecasts of wind speeds at the chosen hub height. The forecasts are derived from the 3-day past data input.

4) *Power Converter*: Wind speed forecasts are converted to wind power using the power curve of country-specific wind turbine. The curve of Enercon turbine E-82 was assumed to be a typical one for the planned Latvian wind parks [21].

The option for geographically differentiated wind speed forecasting is also implemented in the *WIND-LV* tool. As seen from Fig. 1, the total wind power capacity can be broken down up to the level of individual or aggregated wind parks.

5) *Accuracy Evaluator*: Wind power forecasts are compared with actual wind power and the relevant forecasting errors are evaluated.

Verification of the *WIND-LV* tool included the search of tool maximum forecasting time horizon and investigation of forecasting errors for a total of 500 MW.

3.3. Consolidation of System Load and Wind Power Forecasts

The hourly forecasts from the *LOADS-LV* and *WIND-LV* tools are supplied as inputs to the *JOINT-LV* tool, which integrates them into one consolidated load (see

Fig. 1).

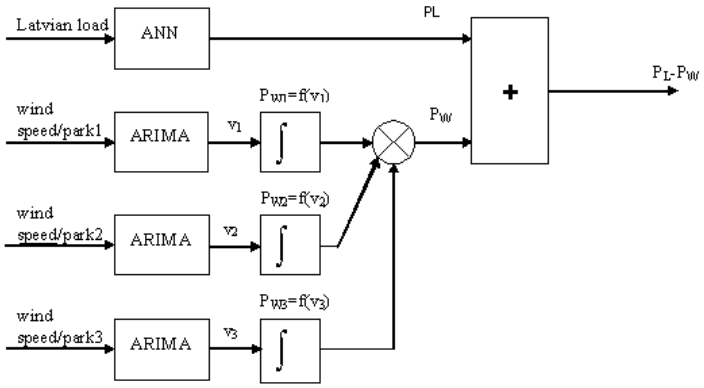

Fig. 1. Structure of the forecasting suit for Latvian power system: P_L – load, P_W – wind power, v – speed.

Here, the investigation was focused on the interplay of forecast errors in order to identify the extent to which they cancel each other. For each pair of hourly load and wind power, the errors are calculated (3) and combined (4) as:

$$\begin{aligned} E_{Li} &= L_i^{act} - L_i^f \\ E_{Wi} &= G_{Wi}^{act} - G_{Wi}^f, \end{aligned} \tag{3}$$

where E_{Li} and E_{Wi} – load and wind power forecasting errors for *i-th* hour;
L_i^{act} L_i^f – actual and forecasted loads for *i-th* hour;
G_{Wi}^{act} G_{Wi}^f – actual and forecasted wind power for *i-th* hour.

$$E_{\Sigma i} = E_{Li} + E_{Wi}, \tag{4}$$

where $E_{\Sigma i}$ – joint forecasting error for *i-th* hour. The joint error effect is achieved when

$$\left|E_{\Sigma i}\right| < \left|E_{Li}\right| + \left|E_{Wi}\right|. \tag{5}$$

The investigation covered 1 month of Latvian PS operation in hypothetical situation with loads from Feb 2012 and planned wind power 500 MW in 2023.

4. RESULTS AND DISCUSSION

The results of load forecasting are presented in Figs. 2–4, wind power forecasting – in Figs. 5 and 6 and combined forecasting results – in Fig. 7.

Figure 2 shows the general view on the accuracy of hourly load forecasts by comparison of forecast and actual load curves. The accuracy can easily be seen to be good, with small errors, without domination of negative or positive forecasts. Figure 3 quantifies the accuracy in terms of mean absolute percentage error (MAPE). The least error appeared in the 24th hour of day cycle with the values of 2.6 % and 2.8 %, while the largest values 5.4 % and 4.5 % were reached in the 6th hour.

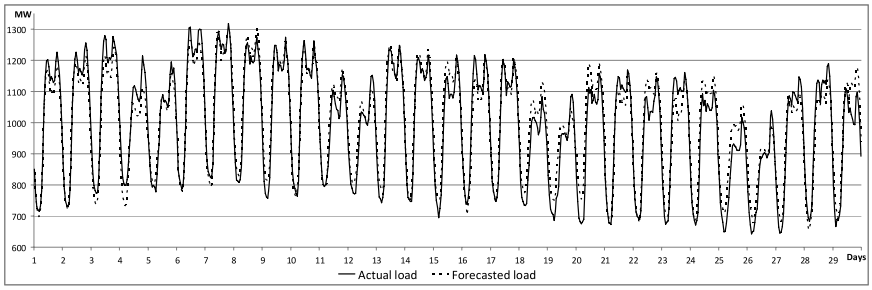

Fig. 2. Latvian hourly load forecasts versus actual loads under next day forecast lead time, Feb 2012.

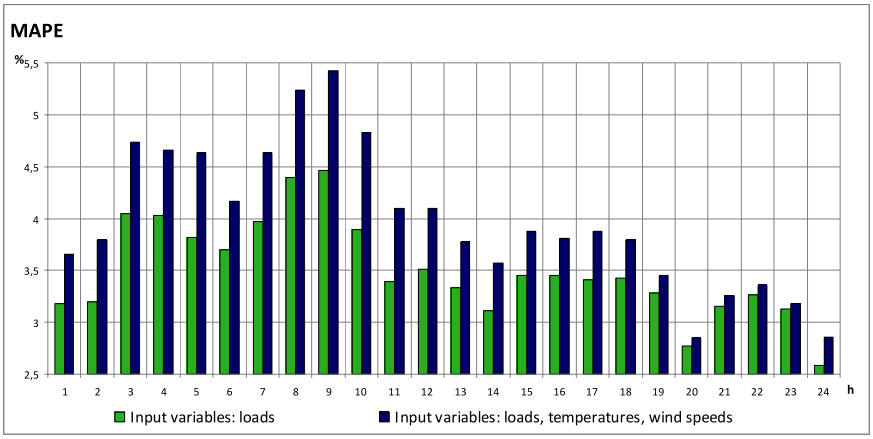

Fig. 3. Latvian load forecasting MAPE as monthly means for each hour of a day cycle under next day forecast lead time, Feb 2012.

Figure 3 also points to an unexpected finding that an increase in the input variable number adversely affects forecasting accuracy. This finding is confirmed in terms of daily MAPE by comparison of forecasts under baseline input (loads only) and extended input (loads, temperatures, wind speeds) in Fig. 3. Such a deterioration can be explained by a negligible or weak correlation:

- 0.04 between loads and temperatures,
- 0.27 between loads and wind speeds,
- 0.35 between wind speeds and temperatures

in the investigation period (4 months).

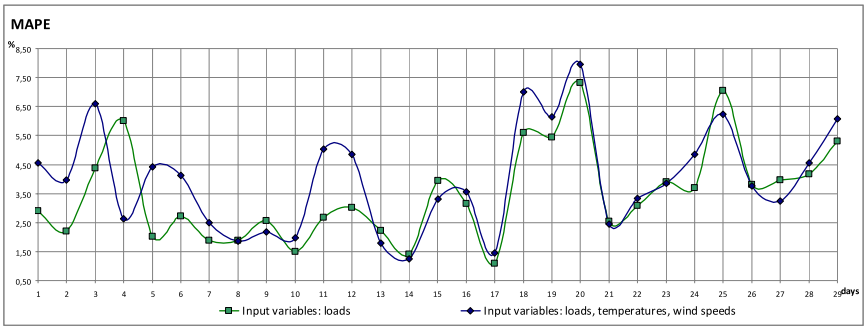

Fig. 4. Daily MAPE of Latvian load forecasting under next day forecast lead time, Feb 2012: 1 – hourly loads as a single input variable; 2 – hourly loads, day type attribute, outdoor temperatures and wind speeds as multiple input variables.

The investigation for maximum forecasting horizon for wind speeds yielded the trend of consistent degradation of accuracy with the increase in forecast lead time. Figure 5 presents the results of this search where forecasting is imitated to be performed each day from 00:00 and 12:00 for 1–12 hours ahead, from 1 Feb to 29 Feb. Thus, every monthly MAE is derived from 58 AE values. Figure 5 demonstrates rather mediocre forecasting capability of ARIMA model, mainly due to the MAE values exceeding 1 m/s for 1–2 h lead time. The acceptable maximum time horizon could be set to no more than 6 h with 1.8 m/s MAE value.

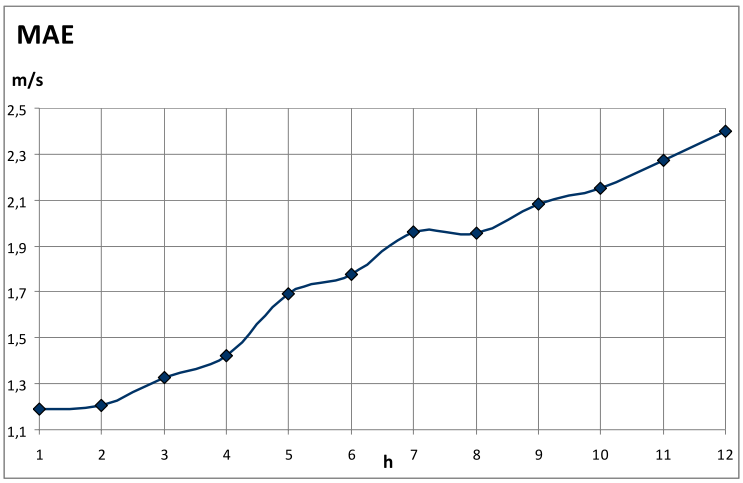

Fig. 5. Monthly MAE of hourly wind speed forecasts under lead time 1–12 h for Riga site, 80-m height, Feb 2012.

Further wind speeds were forecasted with 6-h lead time. Both these forecasts and actual wind speeds (Feb 2012) were converted to hourly wind power values using the aforementioned E-82 power curve for 500 MW capacity rating. The forecasting errors in terms of daily MAPE are presented in Fig. 6. After filtering out 4 values above 20 % as unacceptable from a total of 29 ones, the forecasting accuracy can be considered mediocre but acceptable, with 10–12 % monthly average of remaining 25 daily MAPE.

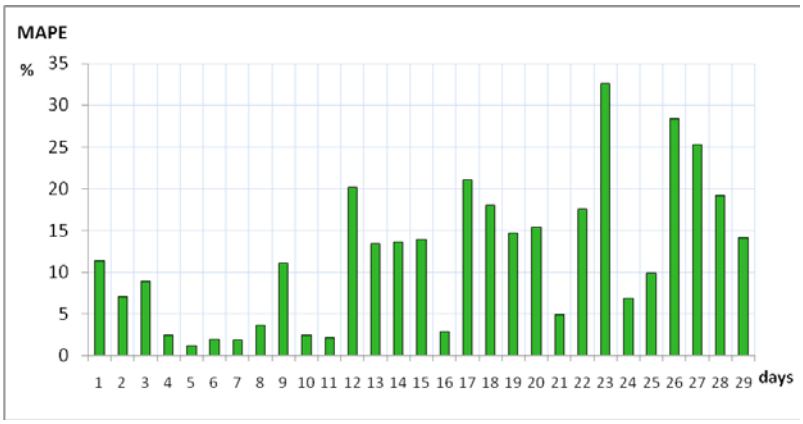

Fig. 6. Daily MAPE of Latvian wind power generation forecasts under 6-h lead time for each hour, Feb 2012 (wind speeds) and 500 MW of planned wind power.

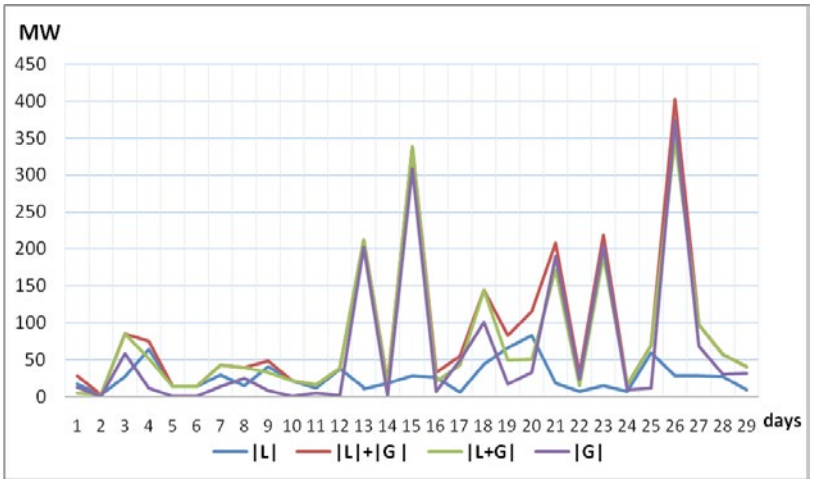

Fig. 7. Combinations of forecasting absolute errors for the 6th hour under weather conditions of Feb 2012 for Latvian maximum load of 825 MW and wind power capacity of 500 MW: L – load, G – wind power.

Results of investigation of forecasting error interplay is presented in Fig. 7. It refers to the 6th hour of each February day when forecasts were made as next-day forecast for load and 6-h lead time forecast for wind power. The contraction of joint error due to the different signs of single errors (for load and wind power) can be observed in certain days but it never falls below any of its single errors. After summarising all 29 days, the contraction of joint error was evaluated to be 13 % as seen from the following:

- 88.6 MW – monthly mean joint error for non-cancelling single errors summed up as |L| +|G|;
- 77.4 MW – monthly mean joint error for cancelling single errors |L + G|:
- 11.2 MW (13 %) – contraction rate.

5. CONCLUSIONS

A new short-term forecasting suit developed for the Latvian power system consisting of *LOADS-LV*, *WIND-LV* and *JOINT-LV* tools for system load, wind power and combined forecasts, respectively, demonstrated acceptable suitability for power system needs, with good performance for load forecasting (ANN model) and mediocre performance for wind speed forecasting (ARIMA model).

Extended input to load forecasting ANN model may lead to less accuracy than baseline input (historical loads only). The reason lies in the weak load correlation with weather temperatures and wind speeds, which hinders the model to capture the true relations between input and output variables.

The combined short-term forecasting of load and wind power brings down the joint forecasting error to appreciable extent.

ACKNOWLEDGEMENTS

The present research has been co-financed by the European Social Fund within the project "Exploration and Solving of Energy Systems' Strategic Development and Management of Technically-Economic Problems", project agreement No. 2013/0011/1DP/1.1.1.2.0/13/APIA/VIAA/028.

REFERENCES

1. Dowds, J., Hines, P., Ryan, T., Buchanan, W., Kirby, E., Apt, J., and Jaramillo, P. (2015). A review of large-scale wind integration studies. *Renewable and Sustainable Energy Rev.*, *49,* 768–794. doi:10.1016/j.rser.2015.04.134.
2. Petrichenko, R., Chuvychin, V., and Sauhats, A. (2013). Coexistence of different load shedding algorithms in interconnected power system. In: *12th International Conference on Environment and Electrical Engineering,* Wroclaw (Poland), art. no. 6549626, (pp. 253–258).
3. Zalostiba, D. (2013). Power system blackout prevention by dangerous overload elimination and fast self-restoration. In: *IEEE European Innovative Smart Grid Technologies Conference*, Copenhagen (Denmark), art. no. 6695371.
4. Augstsprieguma tīkls. [Latvian Transmission System Operator] (2014). *Elektroenerģijas pārvades sistēmas attīstības plāns*. [Development Plan of Transmission Power System]. Riga, 29 p. Available at http://www.ast.lv/files/ast_files/gadaparskzinoj/Latvijas_10GAP_2014.pdf.
5. Litgrid AB (2014). *Development of the Lithuanian Electric Power System and Transmission Grids*. 49 p. Available at http://www.leea.lt/wp-content/uploads/2015/05/Network-development-plan-2015.pdf.
6. EWEA (2014). *Wind Energy Scenarios for 2020*. A report by the European Wind Energy Association. 8 p. Available at http://www.ewea.org/fileadmin/files/library/publications/scenarios/EWEA-Wind-energy-scenarios-2020.pdf.
7. Lee, K.Y., Cha, Y.T., and Park J.H. (1992). Short term load forecasting using an artificial neural network. *IEEE Trans*. PAS ***7*** (1), 124–131.
8. Hippert, H.S., Pedreira, C.E., and Souza, R.C. (2001). Neural networks for short term load forecasting: A review and evaluation. *IEEE Trans. Power Syst.**16***, 44–55.
9. Marin, F.J., Garcia-Lagos, F., Joya, G., and Sandoval, F. (2002). Global model for short-term load forecasting using artificial neural networks. *IEE Proc.-Gener. Transm. Distrib. 149,* 121–125.
10. Costa, A., Crespo, A., Navarro, J., Lizcano, G., Madsen, H., and Feitosa, E. (2008). A review on the young history of the wind power short-term prediction. *Renewable and Sustainable Energy Rev.* ***12***, 1725–1744.
11. Milligan, M. (2003). *Wind Power Plants and System Operation in the Hourly Time Domain*. Austin (Texas, USA), Windpower 2003, 23 p. NREL/CP-500-33955. Available at http://www.nrel.gov/publications/.
12. Cadenas, E., and Rivera, W. (2007). Wind speed forecasting in the South Coast of Oaxaca, México. *Renewable Energy* ***32***, 2116–2128.
13. Kavasseri, R. G., and Seetharaman, K. (2009). Day-ahead wind speed forecasting using f-ARIMA models. *IEEE Tran. Renewable Energy 34,* 1388–1393. DOE:10.1016/j.renene.2008.09.006.

14. Shukur, O. B., and Lee M. H. (2015). Daily wind speed forecasting through hybrid KF-ANN model based on ARIMA. *Renewable Energy* ***76***, 637–647.
15. Cadenas, E., and Rivera, W. (2010). Wind speed forecasting in three different regions of Mexico, using a hybrid ARIMA–ANN model. *Renewable Energy* ***35***, 2732–2738
16. Augstsprieguma tīkls. [Latvian Transmission System Operator] (2015). *Demand, net exchange and production.* Available at http://www.ast.lv/eng/power_system/archive.
17. Riga Actual Weather Archive. (2015). Available athttp://www.meteoprog.lv/en/weather/Riga/.
18. Khwaja, A.S., Naeem., M., Anpalagan A., Venetsanopoulos, A., and Venkatesh, B. (2015). Improved short-term load forecasting using bagged neural networks. *Electr. Power Syst. Res*. ***125***, 109–115.
19. Bañuelos-Ruedas, F., Angeles-Camacho, C., and Rios-Marcuello, S. (2011). Methodologies used in the extrapolation of wind speed data at different heights and its impact in the wind energy resource assessment in a region. In: *Wind Farm – Technical Regulations, Potential Estimation and Siting Assessment* / Suvire G. O (Ed.): InTech, 246 p. DOI:10.5772/673.
20. Radziukynas, V., and Klementavicius, A. (2014). Short-term wind speed forecasting with ARIMA model. In: *55th International Scientific Conference on Power and Electrical Engineering of Riga Technical University (RTUCON),* Riga (Latvia), (pp. 145–149). Doi 10.1109/RTUCON.2014.6998223.
21. ENERCON. (2015). Enercon Wind Turbines. Product overview.

SLODZES UN VĒJA JAUDAS ĪSTERMIŅA PROGNOZĒŠANA LATVIJAS ENERGOSISTĒMAI: IZSTRĀDĀTĀS METODIKAS PRECIZITĀTE UN VEIKTSPĒJA

V. Radziukynas, A. Klementavičius

Kopsavilkums

Rakstā veikta Latvijas energosistēmas slodzes un vēja jaudas īstermiņa prognozēšana. Analizēti iegūtie rezultāti. Energosistēmas slodzi un vēja jaudu var prognozēt, izmantojot ANN un ARIMA modeļus. Prognozēšanas precizitāti var novērtēt ar vidējo absolūto kļūdu un vidējo absolūto kļūdu procentos. Tika pētīts kā slodzes prognozēšanas kļūdu ietekmē dažādi energosistēmas parametri. Izmantojot Latvijas energosistēmas vēsturiskos parametrus (2011.g.), tika noteiktas ikstundas slodzes un vēja jaudas prognozēšanas kļūdas, kā arī prognozēta plānota vēja jauda 2023. gadam.

24.07.2015.

LATVIAN JOURNAL OF PHYSICS AND TECHNICAL SCIENCES
2016, N 2

DOI: 10.1515/lpts-2016-0009

TIME AND FREQUENCY SYNCHRONIZATION ON THE VIRAC RADIO TELESCOPE RT-32

V. Bezrukovs

Engineering Research Institute "Ventspils International
Radio Astronomy Centre" of Ventspils University College (VIRAC)

101 Inzenieru Str., Ventspils, LV-3601, LATVIA
vladislavsb@venta.lv

One of the main research directions of Ventspils International Radio Astronomy Centre (VIRAC) is radio astronomy and astrophysics. The instrumental base for the centre comprised two fully steerable parabolic antennas, RT-16 and RT-32 (i.e. with the mirror diameter of 16 m and 32 m). After long reconstruction, radio telescope RT-32 is currently equipped with the receiving and data acquisition systems that allow observing in a wide frequency range from 327 MHz to 9 GHz. New Antenna Control Unit (ACU) allows stable, fast and precise pointing of antenna. Time and frequency distribution service provide 5, 10 and 100 MHz reference frequency, 1PPS signals and precise time stamps by NTP protocol and in the IRIG-B format by coaxial cable.

For the radio astronomical observations, main requirement of spatially Very Long Base Line Interferometric (VLBI) observations for the observatory is precise synchronization of the received and sampled data and linking to the exact time stamps. During October 2015, radio telescope RT-32 performance was tested in several successful VLBI experiments. The obtained results confirm the efficiency of the chosen methods of synchronization and the ability to reproduce them on similar antennas.

Keywords: *radio telescope, antenna control system***,** *time and frequency synchronization*

1. INTRODUCTION

One of the main research directions of Ventspils International Radio Astronomy Centre (VIRAC) is radio astronomy and astrophysics. The instrumental base for the centre comprised two fully steerable parabolic antennas, RT-16 and RT-32 (i.e. with the mirror diameter of 16 m and 32 m). The telescopes were built in the 60s of the last century and used for military purposes. The reconstruction and instrumental refurbishment carried out for last years by VIRAC engineering team and various Latvian and international contractors made it possible to use these radio telescopes for the international scale fundamental and applied research in the field of radio

astronomy. The most important aspect of the work is participation of RT-32 in the VLBI (Very Long Baseline Interferometry) international experiments. To use radio telescope RT-32 as a stable and reliable VLBI station it must comply with several performance criteria: fast, stable and precise pointing and tracking, receiver and data acquisition system compatible with VLBI standards and properly organised synchronization of all components.

2. SCHEMATIC DIAGRAM OF THE RADIO TELESCOPE RT-32

Operation of the radio telescope depends on the smooth and coordinated operation of various internal systems. Overall, schematic diagram of radio telescope RT-32 components is presented in Fig 1. Conventionally, a radio telescope operation can be divided into the following groups:

- Systems intended for the registration of a radio signal, digitizing the data and writing them on the media.
- Antenna Motion Control Systems, including monitoring and control of motors, the calculation of antenna pointing and movement trajectories generation, controlling of antenna position ad status sensors.
- Secondary systems for the monitoring of the weather situation, logging of antenna status, recorded data quality and other.
- However, for the successful functioning of a radio telescope as an instrument able to solve scientific and applied goals, a stable and highly accurate synchronization of all systems is needed. For these purposes, on the RT-32 time and frequency distribution service are used.

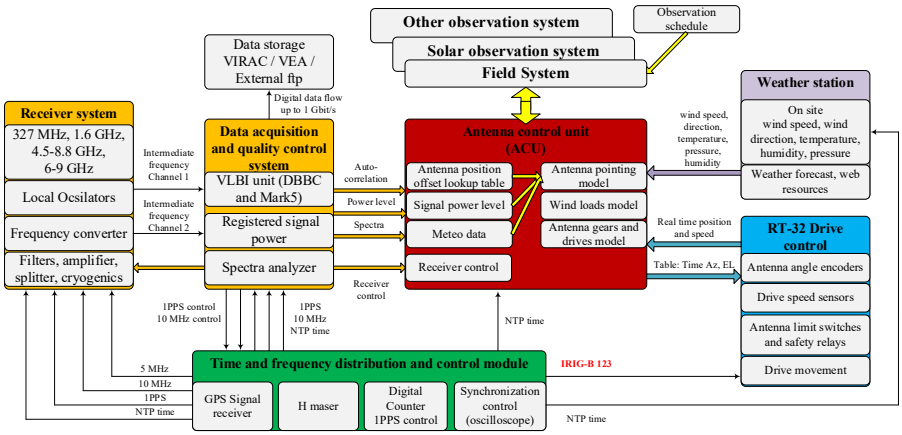

Fig. 1. Schematic diagram of systems incorporated in the radio telescope RT-32.

3. TIME AND FREQUENCY DISTRIBUTION AND CONTROL SERVICES

For the radio astronomical observations, the main requirement of spatially Very Long Base Line Interferometric (VLBI) observations for the observatory is precise synchronization of the received and sampled data and linking to the exact time

stamps. Precise time is also needed for accurate calculations of current coordinates of the antenna and the observed objects. As the frequency and time standard for RT-32 an active hydrogen maser Quartz CH1-75A is used, which generates reference frequencies of 5, 10 100 MHz and 1PPS signal. 5 and 10 MHz reference frequency are required for radio telescope receiver units, enabling stable work of their Local Oscillators. Additionally, 10 MHz sinusoidal reference signal is supplied to the radio telescope digital backbends (DBBC and TN-6) and ensures coherent data digitalization.

For the setting and checking the time scale "Symmetricom XL-GPS Time and Frequency" system is employed. This GPS receiver generates one-second pulses based on the signals from GPS satellites. In addition, it has an NTP-server providing accurate time transfer to all devices of the telescope via a LAN (Local Area Network).

To control the synchronization of the observatory acquisition systems, a four-channel oscilloscope R&S RTO 1014 is applied, which displays the PPS signals from GPS, DBBC, Mk5b, 10 MHz from DBBC and 10 MHz from hydrogen frequency and time standard. In the case when one of the devices loses synchronization, this will be easily detected on the oscilloscope's display.

For long-term control of active hydrogen maser Quartz CH1-75A performance and stability, 1PPS signal from CH1-75A and 1PPS signal from GPS receiver are connected to the digital counter Agilent 53132A, which calculates difference between these signals. Digital counter sends this data to the observatory server by GPIB-Ethernet interface.

4. RECEIVING AND DATA ACQUISITION SYSTEMS OF RADIO TELESCOPE RT-32

Selection of receiving systems is determined by scientific and applied tasks, which are topical for VIRAC observatory. At present, VIRAC works in the following directions:

- investigation into the motion parameters of objects in the near-Earth space (space debris, satellites, asteroids) and planets;
- studying the Earth's ionosphere;
- studying the solar radio emission;
- observations in the international VLBI-networks, including the European VLBI network (EVN).

To achieve these objectives, it is possible to use the following receiving systems:

- 327 MHz (92 cm, P band) – primary focus, VLBI;
- 1.6 GHz (18 cm, L band) – secondary focus, GNSS satellites tracking, VLBI;
- 4.5–8.8 GHz (6 cm; C, M, X bands) – secondary focus, VLBI, space debris radio location;
- 6.9–9.3 GHz (3.7–4.2 cm) – secondary focus, solar spectro-polarimetric studies [1], [2].

For the receivers 327 MHz and 4.5-8.8 GHz the signal generator Rohde&Schwarz (R&S) SMP 04 is used as the Local Oscillator (LO) synchronized by a hydrogen frequency standard.

For digitalization and registration of the received signal, at the RT-32 two independent systems are used: TN-16 – the NIRFI terminal for signal record with a sampling frequency up to 16 MHz (developed at the Radiophysical Research Institute, Nizhny Novgorod) and DBBC – the Digital Base Band Converter (developed in the last decade at the Institute of Radioastronomy, Noto) as a generic, modular radio-astronomical data acquisition architecture to be used inside the European VLBI community [3].

The signals applied at the inputs of TN-16: the analogue input signal, clock signal (up to 16 MHz), 1PPS (pulse-per-second) reference signal from the hydrogen frequency standard and 5 V from a DC voltage.

The DBBC unit is composed of a base box (containing power supply, control computer, clock distribution and JTAG interface), and a stack of small modular boards, which can be composed according to the user needs. The first and the last modules in the system (FILA boards) provide the control signal distribution, a DAC for monitoring, and the electric interface to the standard VSI bus to the VLBI data recorder. The digitized signal is fed to Mk5b by VSI-H interface. For its operation, DBBC requires the following input signals: 10 MHz reference and 1PPS (supplied by a hydrogen frequency standard). For control of the input signal, the internal synchronization and sampled band DBBC are fitted with the following outputs: “RF out” and “RF monitor” for each of the four Conditioning Modules, “1 PPS out”, “10 MHz out” and “AnalogOut”, which allow checking all sampled channels.

The system Mk5b (connected to DBBC through VSI-H cable) is used for recording the sampled data flow. For synchronization, Mk5b uses 1PPS and 32MHz signals obtained through VSI-H interface from the DBBC [1], [2], [3].

5. ANTENNA MOTION CONTROL SYSTEMS

In the radio telescopes RT-32 and RT-16 for the antenna motion control, the Antenna Control Unit (ACU) developed by MT Mechatronics Company is used.

The purpose of the ACU is to provide a high quality stable tracking behaviour enabling the scientist to track star objects, the sun or satellites. New ACU system was installed during refurbishment of these radio telescopes, which was finished at the end of summer 2015. The old motors and drive system were replaced, and telescopes were equipped with a new servo system. At present, the telescope axes are controlled by the ACU, which consists of several modules and interfaces.

The software comprises the following basic parts:

- Facility Control Module: Temperature Sensors, Safety System, Fieldbus and Power Status;
- HMI Module: Handling of HMI interfaces;
- Axis Module: Trajectory Generator, Axis Command Handling, Axis State Machine;

- Pointing and Tracking Module: Program Tracking, TLE Tracking, Time System.

External Interfaces to the software are:

- The EtherCAT Field Bus controller that communicates with all drive system components, e.g. motor modules, encoder systems, serial interfaces and MTM clock module.
- The TcpIp Interface that handles the communication with different HMI visualizations and radio telescope remote connection.
- Beckhoff ADS internal connection that is used for diagnosis, logging and debugging [4].

The ACU module is integrated in the radio telescope control system (RT-Control), which coordinates work of all radio telescope components. One of the major parts of RT-Control is a Field System (FS) – software unit developed by NASA. The FS control while the observational process: defines targets for ACU, sets working frequencies in the DBBC, sets recording time and mode in the Mk5, additionally records weather conditions received from a local meteorological station. As all mentioned units should work synchronously, correctly organised time synchronization is of particular importance. In the VIRAC observatory, time signals are distributed from a local NTP timeserver. In the Windows based computers, NTP time is set by "SP TymeSync" software package written by Alexander Panchenko. In turn, Linux machines use their own NTP daemons.

In addition, to provide reliability, ACU obtains time directly from a GPS receiver using IRIG-B 123 standard format for transferring timing information by coaxial cable.

6. CONCLUSIONS

After long reconstruction, the radio telescope RT-32 is currently equipped with the receiving and data acquisition systems that allow observing in a wide frequency range from 327 MHz to 9 GHz. New ACU allows stable, fast and precise pointing of antenna. Time and frequency distribution service provides 5, 10 and 100 MHz reference frequency, 1PPS signals and price time stamps by the NTP server and in the IRIG-B format by coaxial cable.

During October 2015, the performance of radio telescope RT-32 was tested in several successful experiments: GNSS satellite tracking tests; VLBI observations in frequency bands of 1.6, 5, 6.7 and 8 GHz in collaboration with EVN network; VLBI observations of GNSS satellites at 1.6 GHz in collaboration with the Radiophysical Research Institute, Nizhny Novgorod.

The obtained results confirm the efficiency of the chosen methods of synchronization and can be reproduced on similar antennas.

ACKNOWLEDGEMENTS

The present research has been conducted as part of research project No. L-KC-11-0006 funded by the European Regional Development Fund. The project

is implemented by Ltd. "ORAM Mobile" in collaboration with Ventspils University College. The author would like to express his gratitude to VIRAC engineering and research team for their hard work devoted to radio telescope reconstruction as well as to MT Mechatronics team.

REFERENCES

1. Bezrukovs, V., Shmeld, I., Nechaeva, M., Trokss, J., Bezrukovs, D., Klapers, M., Berzins, A., and Lesins, A. (2012). Receiving and data acquisition systems of RT-32 for VLBI observations. *Latvian Journal of Physics and Technical Sciences* ***6*** (2), 30–42.
2. Bezrukovs, D. (2013). Spectral polarimetric observations of the Sun by VIRAC RT-32 radiotelescope. *Baltic Astronomy* ***22*** (1).
3. Tuccari, G., Alef, W., Bertarini, A., Buttaccio, S., Comoretto, G., Graham, D., Meidhart, A., Platania, P., Russo, A., Roy, A., Wunderlich, M., Zeithoefler, R., and Xiang, Y. (2010). DBBC2 backend: Status and development plan. In: *IVS General Meeting Proceedings.*
4. Petersen, A., Hartmann, S., and Tschetschel R. (2015). Ventspils RT-16 / RT-32 Servo. *Operational Manual.* VTP2-DOC-34100-01.

VSRC RADIO TELESKOPA RT-32 LAIKA UN FREKVENCES SINHRONIZĀCIJA

V. Bezrukovs

K o p s a v i l k u m s

Viens no Ventspils Starptautiskā Radio Astronomijas Centra (VSRC) galvenajiem darbības virzieniem ir radio astronomija un astrofizika. VSRC instrumentālo bāzi veido divas pilnīgi grozāmas paraboliskas antenas RT-16 un RT-32 (ar spoguļa diametriem 16 m un 32 m). Pēc ilgas rekonstrukcijas, radioteleskops RT-32 šobrīd ir aprīkots ar uztveršanas un datu reģistrācijas sistēmu, kas ļauj veikt novērojumus plašā frekvenču diapazonā no 327 MHz līdz 9 GHz. Jauna antenas vadības sistēma (ACU) ļauj nodrošināt stabilu, ātru un precīzu antenas uzvadīšanu un sekošanu. Laika un frekvences dienests antenas mezgliem nodrošina 5, 10 un 100 MHz referenču signālus, vienas sekundes (1PPS) impulsus un precīzus laika mārkerus ar NTP protokolu un IRIG-B formātu caur koaksiālo kabeli.

Radio astronomiskajiem novērojumiem, īpaši lielas bāzes interferometriskiem (VLBI) novērojumiem, galvenā prasība ir reģistrēto signālu un nociparoto datu sinhronizācija un nodrošināšana ar precīziem laika mārkeriem.

No 2015. gada oktobra radio teleskopa RT-32 veiktspēja tika pārbaudīta vairākos veiksmīgos starptautiskos VLBI eksperimentos. Iegūtie rezultāti apstiprina izvēlēto sinhronizācijas metožu efektivitāti un iespēju reproducēt tos uz līdzīgām antenām.

02.11.2015.

LATVIAN JOURNAL OF PHYSICS AND TECHNICAL SCIENCES
2016, N 2

DOI: 10.1515/lpts-2016-0010

EXPERIMENTAL AND NUMERICAL ANALYSIS OF AIR FLOW, HEAT TRANSFER AND THERMAL COMFORT IN BUILDINGS WITH DIFFERENT HEATING SYSTEMS

A. Sabanskis, J. Virbulis

Laboratory for Mathematical Modelling of Technological and Environmental Processes, University of Latvia,
8 Zellu Str., Riga LV-1002, LATVIA

Monitoring of temperature, humidity and air flow velocity is performed in 5 experimental buildings with the inner size of 3x3x3 m^3 located in Riga, Latvia. The buildings are equipped with different heating systems, such as an air-air heat pump, air-water heat pump, capillary heating mat on the ceiling and electric heater. Numerical simulation of air flow and heat transfer by convection, conduction and radiation is carried out using OpenFOAM software and compared with experimental data. Results are analysed regarding the temperature and air flow distribution as well as thermal comfort.

Keywords**:** *experimental buildings, monitoring system, numerical simulation, OpenFOAM, thermal comfort.*

1. INTRODUCTION

Under growing demand for energy efficiency for building design and introduction of new alternative concepts for heating, the increased attention should be devoted to ensure the indoor environment quality.

In addition to the different types of radiant heating [1], the cost and energy efficient air-air heat pumps play an important role also in cold climate conditions [2]. Air-air heat pumps include controlled ventilation systems ensuring necessary air quality. Particular heating systems produce different flow and temperature distributions in the room, influencing both heating performance and thermal comfort.

A review of general and local thermal comfort models and elaborated standards in indoor ambiences is given in [3]. Popular standards such as ASHRAE 55-2004 and ISO 7730 are relatively compatible, in the present article the thermal comfort conditions are analysed as described in standard ISO 7730:2005 [4]. Standards suggest that thermal comfort can be expressed in terms of Predicted Mean Vote and Predicted Percentage Dissatisfied regarding the drought rate, vertical air temperature difference, warm or cool floor and radiant asymmetry.

Numerical simulations are often used for the investigation of heating and

cooling systems in buildings. Main advantages of simulations are the existence of calculated values of air flow and temperature in every point of the considered domain as well as the possibility to study the parameters already in the planning stage. However, experiments are utmost necessary to validate the models; therefore, experimental and numerical investigations are often combined [5], [6], [7].

In the present article, several radiant and air heating systems are investigated and compared regarding the flow pattern, temperature distribution, integral thermal behaviour and thermal comfort.

2. EXPERIMENTAL ENVIRONMENT

Five test stands with equal size and orientation in space (window on the south facade, doors on the north) have been built in the Botanical garden of the University of Latvia, Riga, Latvia [8]. They are denoted as AER, CER, EXP, LOG and PLY, which stand for the materials used for the walls – aerated concrete blocks, perforated ceramic blocks, perforated ceramic blocks filled with insulating granules, laminated beams and modular plywood panels, respectively. The walls are constructed to have the same thermal transmittance (U-value) of 0.16 W/m^{2}K. Internal size of each stand is 3x3x3 m^3. Internal components of the stands with the considered heating systems are shown in *Fig. 1*. The geometry of the system with a capillary heating mat on the ceiling is the same as for the air-water heat pump (*Fig. 1b*).

The following heating systems were used: air-air heat pump in LOG and AER, air-water heat pump in PLY, air-water heat pump with a capillary heating mat on the ceiling in EXP and electric heater in CER. An air-air heat pump was installed in all buildings and used for ventilation only in the PLY, EXP and CER stands. The main air circulation is between the air inlet and air feedback in the internal block of the air-air heat pump. Some amount of fresh air is mixed to this flow and the same amount of air is leaving through the ventilation outlet placed over the window.

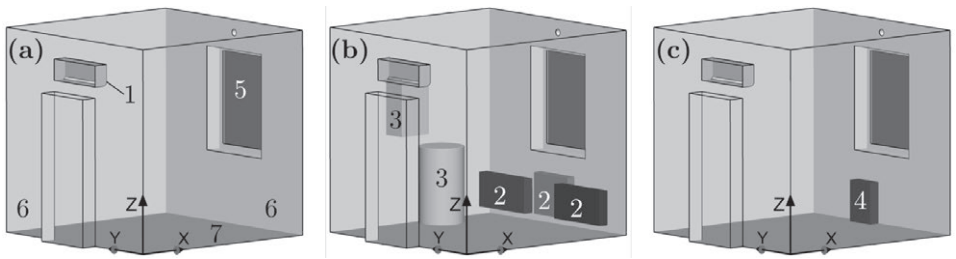

Fig. 1. Geometry of the systems with (a) air-air heat pump (1 – internal block), (b) air-water heat pump (2 – convectors; 3 – internal blocks) and (c) electric heater (4). Other denotations: 5 – window; 6 – walls; 7 – floor. Doors are located opposite the window.

3. MEASUREMENT SYSTEM

Identical sensors are installed in all test stands and are linked to the web-based data acquisition system for the automatic collection of data [9]. In the present study,

the temperature measurements in the middle of the room in 5 points at different vertical positions (0.1 m, 0.6 m, 1.1 m, 1.7 m from floor and 0.1 m from ceiling) are used for the comparison with the simulated temperature distribution. Repeatability of the used temperature sensors is ±0.1 °C, and the accuracy is ±0.3 °C [10].

4. NUMERICAL MODEL

For the numerical calculations of air flow and heat transfer, the modified calculation program chtMultiRegionSimpleFoam from the OpenFOAM version 2.3 open source code library [11] is used. Temperature was calculated in the air and solid domains (walls, ceiling, floor, window, doors).

The air flow is considered stationary and is described by the continuity and momentum equations. Air density ρ is calculated by the ideal gas law. The SST k-ω turbulence model with default model coefficients is used [11], [12], [13]. The no-slip condition has been applied at the solid walls. The velocity $\vec{U}$ at the ventilation outlet is specified according to the desired air exchange rate.

The enthalpy formulation is used for the calculations of energy transfer in the air and solid domains [11]. A constant outdoor temperature is applied at the external surfaces. Thermal radiation is calculated by the view factor model, which takes into account visibility of the surface elements, as well as their temperature and emissivity.

The thermal conductivities of solid domains were taken from [14] where the effective conductivity values were calculated to obtain the U-value of 0.16 W/m^{2}K. The following values of κ (in mW/(m·K)) were used: 91.8 for walls (EXP stand), 66.2 and 48.2 for the two-layered ceiling, 82.971 and 50.805 for the two-layered floor, 35.433 for the window, 62.532 for doors.

The balance of mass flow rate and heat fluxes has to be satisfied for the converged stationary solutions. The mass flow rate Q in kg/s through surface S is calculated by integrating the mass flux $\rho\vec{U}$.

There is one air inlet (denoted by "i") and two outlets (ventilation denoted by "v" and air feedback denoted by "f"). The mass conservation law reads $Q_i+Q_v+Q_f=0$, where the signs of the mass flow rates are $Q_i>0$, $Q_v<0$ and $Q_f<0$.

The conductive heat flux P_q through surface S is calculated using the temperature gradient. The net heat flux P_r radiated by surface S is computed by integrating the net radiation heat flux density. The convective heat flux P_c is calculated using 0°C as the reference temperature. The heater power is calculated as the sum of the conductive (P_q) and radiation (P_r) heat fluxes: $P_h=P_q+P_r$.

Since the temperature field inside the heaters is not considered, the surface temperature of the heaters is specified and the power is calculated during the post-processing stage. The used method allows describing cases with a heater turned off by setting $P_q=0$. In this case, $P_h=P_r$, which depends on the thermal conditions and in a general case does not vanish.

The power P_{aa} consumed by the air-air heat pump is calculated as follows:

$$P_{aa} = P_{c,i} + P_{c,v} + P_{c,\text{out}}, \qquad P_{c,\text{out}} = \int_S \rho\, c_p\, (T_{\text{out}} - T_0)\, \vec{U}\, d\vec{S},$$

where the convective heat fluxes P_c are calculated at the inlet and outlets, as defined previously. The signs are $P_{c,i} > 0$, $P_{c,v} < 0$ and $P_{c,\text{out}} < 0$. For the cases when the air-air heat pump is only used for ventilation, $P_{aa} = 0$ and the temperature at the inlet is calculated as follows: $T_i = -\left(P_{c,v} + P_{c,\text{out}}\right)/\left(c_p Q_i\right)$.

The mean radiant temperature used for the analysis of thermal comfort is calculated by the equation

$$\text{MRT} = \left(\sum_{i=1}^{N} F_{0i} T_i^4\right)^{1/4},$$

where F_{0i} is the diffuse view factor and N is the number of the radiating elements.

For the thermal comfort analysis, the difference between the MRT on the opposite sides of an imaginary plane element is calculated: $\Delta\text{MRT}_{\text{ud}}$ (up-down) in +z and –z direction, $\Delta\text{MRT}_{\text{fb}}$ in +x and –x direction, and $\Delta\text{MRT}_{\text{lr}}$ in +y and –y direction.

5. RESULTS AND DISCUSSION

5.1. Experiments

The previously measured air exchange rates in the test stands reported in [8] are in the range from 0.43 to 0.50 h^{-1}. It has also been verified that more than 90 % of the air exchange is due to air flow through the ventilation opening.

Since the simulations are stationary, the modelling results should be compared with experiments carried out under utmost steady conditions. To obtain such experimental results, louvers of the air-air heat pump were fixed in all test stands. The time-averaged temperatures in the middle of the stands at different vertical positions are shown in *Fig. 4*. Averaging was done on 2nd December 2014, over 9.2 h. During the experiment the temperature outside varied between -6°C and -8°C and solar radiation from cloudy sky changed between 0.5 W/m^2 in the night and up to 40 W/m^2 during the day, so the solar heat sources through the window were neglected.

5.2. Simulations

5.2.1. Summary of Considered Cases

In *Table 1*, the cases considered in simulations are summarised. The parameters are: T_i – temperature at inlet of air-air heat pump, U_i – inlet velocity, α_i – direction of inlet with respect to x axis ($\alpha_i = 0°$ corresponds to horizontal inflow, $\alpha_i = 90°$ – to inflow vertically downwards), P – heating power, T_{avg} – average temperature of the air, T_{floor} – average temperature of the floor. The temperature at the external walls of solid domains was set to -6°C and air exchange rate – to 0.45 h^{-1}. Cases aa1, el1, wa1 and cm1 correspond to the conditions in experiments and other cases study the effect

of inlet velocity and direction.

Table 1

Summary of the Modelled Cases

Case	Heating	T_i, °C	U_i, m/s	α_i, °	P, W	T_{avg}, °C	T_{floor}, °C
aa1	air-air	22.9	2.0	70	415	19.7	18.0
aa2	air-air	22.9	2.5	70	435	20.2	19.1
aa3	air-air	22.9	1.6	60	410	19.3	16.5
el1	electric	17.8	2.0	70	420	18.5	18.1
el2	electric	17.7	4.0	60	403	18.1	17.6
wa1	water-air	19.2	2.0	70	436	19.9	19.4
wa2	water-air	19.5	3.1	60	436	19.9	19.4
cm1	ceiling mat	15.4	3.4	60	403	15.4	15.2

5.2.2. Mesh Generation and Numerical Aspects

3D hexahedra-dominant finite volume meshes for all the configurations were created using the OpenFOAM mesh generator snappyHexMesh [11]. An example of mesh for the case with water-air heat pump in different cross-section planes of air domain is shown in *Fig. 2*. Thickness of cells at the solid walls is 10 mm, which increases by a factor of 1.15 until a bulk cell size of 40 mm is reached.

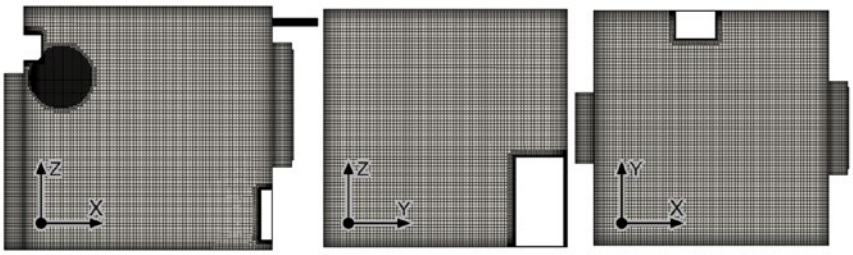

Fig. 2. Example of finite volume mesh for system with water-air heat pump, 2.0 million cells. The refinement region near the inlet of air-air heat pump appears black in the figure.

Additional mesh refinement is applied in the vicinity of the inlet of the air-air heat pump (black region in *Fig. 2*), with the cell size being 5 mm in the immediate vicinity of the heat pump, and 10 mm in the region of airflow from the inlet.

5.2.3. Air Flow and Temperature Distributions

Figure 3 shows the calculated velocity and temperature fields in the air for all considered cases. The white isolines of air flow velocity at U=0.2 m/s help distinguish between regions of high and low velocity. In all cases, contra-clockwise vortex with maximum velocity at inlet is generated. The shape of the vortex clearly correlates with the inflow angle and velocity. For a large angle (aa1, aa2, el1, wa1) the jet reaches the floor closer to the inlet side. The same is true for a larger velocity

(e.g. compare aa1 to aa2). Comparing the cases with the same inlet conditions (aa1, el1, wa1) the effect of the heating system can be seen as well.

Equal inlet temperature of 22.9 °C was used for the cases (aa1)–(aa3), while the inlet velocity and angle was varied. For a sufficiently large inlet velocity (aa1) and (aa2) hot air from the inlet reaches the floor, while in the case of reduced velocity (aa3) the buoyancy effects prevent this and the average floor temperature is lower by 1.5–2.6 °C. The different inlet velocities also affect the convective heat gain, and, as a result, the average air temperature. The high inflow rate (aa2) results in a better mixing of the air and reduces temperature variations.

In case of the capillary heating mat on the ceiling (cm1), the air temperature inside the room is the most homogeneous of all cases. The cases with the electric heater (el1 and el2) show strong upward flow which is affected by the inlet velocity – for small velocity (el1) air from the heater rises vertically upwards, while for twice as high velocity (el2) it deviates from the vertical direction. The temperature at the heater surfaces is 63.2 °C and 56.9 °C for el1 and el2, respectively.

The cases with the water-air heat pump (wa1) and (wa2) behave similarly as the cases with the electric heater – for the large inflow velocity the hot air is dragged along and a distinct vortex is formed. The temperature distributions in the room are more homogeneous than in the cases with electric heaters, the temperature at the heater surfaces is 33.7 °C and 31.9 °C for (wa1) and (wa2), respectively.

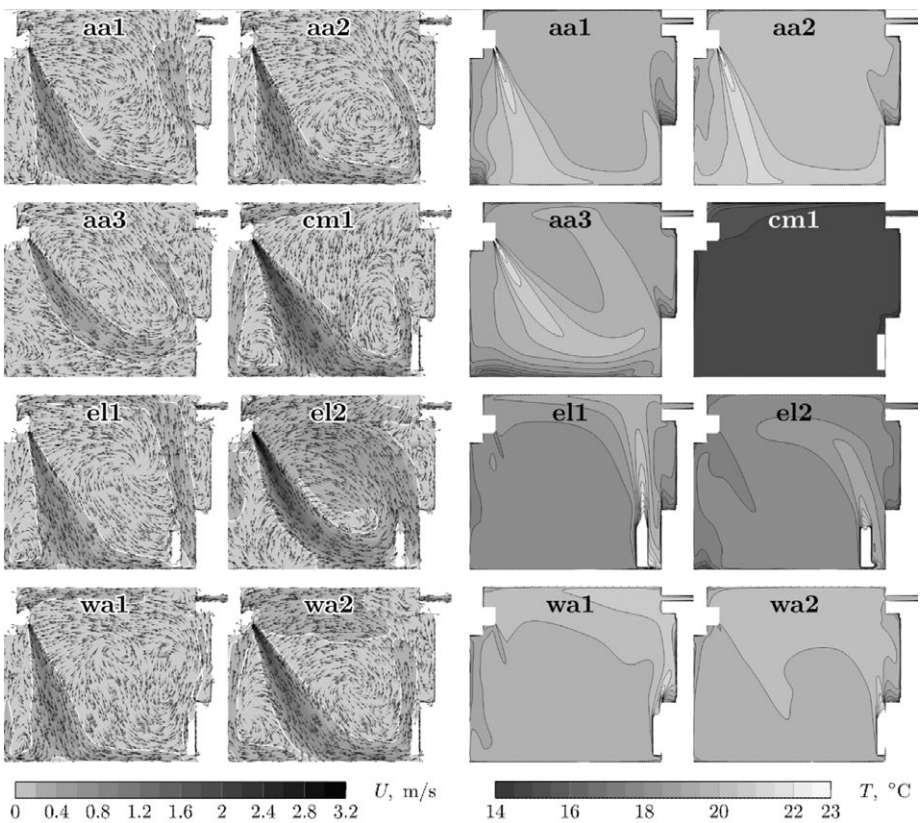

Fig. 3. Left: velocity field and isoline of U=0.2 "m/s" (white); right: temperature field (spacing between isolines is 0.5 °C).

5.2.4. Integral Thermal Analysis

Contrary to measurements in 5 points, the simulation results provide temperature and heat flux values in every point of the considered domain. Therefore, integral analysis can be done easily by averaging the calculated values over a volume or particular surfaces. The integral heat fluxes are summarised in *Table 2* where heat gains are positive and heat losses – negative. The calculated balance of all the heat fluxes SUM does not exceed 4 W or 1% in any case. The heating power of the air-air heat pump can be calculated as a sum of inflow and feedback heat fluxes.

The power used for heating is approximately the same for all cases in the range from 403 W (cm1) to 436 W (wa1). The mean air temperature varies between 15.4 °C (cm1) to 20.2 °C (aa2). However, there is no distinct correlation between the heater power and the air temperature. The air temperature depends more on the heating system, i.e. how efficient the heat is mixed into the air before leaving the room through construction elements and ventilation. The heat losses for different systems are compared using a kind of integral U-value calculated as the ratio of the heating power to the temperature difference (mean air temperature minus outdoor temperature) per m^2. It is 0.299–0.307 W/m^2K for the air-air system, 0.312 W/m^2K for the air-water heat pump system, 0.310–0.317 W/m^2K for the electrical heater and 0.349 W/m^2K for the ceiling mat. In the first case, the warm air is directly mixed into the convective vortex; in the case of the ceiling mat, mixing is smaller due to slow velocity at the ceiling and stratification of temperature.

Table 2

Integral Heat Fluxes in W

Case	Inflow	Ventilation	Feedback	Ceiling	Floor	Window	Doors	Walls	Heater	SUM
aa1	2203	-77	-1818	-39	-41	-27	-34	-171	-	-4
aa2	2753	-79	-2348	-40	-43	-27	-36	-177	-	3
aa3	1879	-75	-1499	-38	-39	-26	-33	-165	-	4
el1	1743	-77	-1768	-39	-41	-27	-34	-174	420	3
el2	3682	-70	-3707	-38	-41	-26	-33	-169	403	1
wa1	1871	-81	-1895	-41	-44	-28	-36	-184	436	-2
wa2	3168	-78	-3192	-41	-44	-28	-36	-183	436	2
cm1	2778	-62	-2806	-67	-37	-24	-30	-152	403	3

5.2.5. Comparison with Experiment

The comparison of the calculated vertical temperature distributions in the centre of the test stands with experiment is given in *Fig. 4*. Since the same heating conditions with the air-air heat pump were used in LOG and AER stands, the same simulation result is used in both comparisons. Despite the identical heating conditions in the AER and LOG stands, the measured temperature distribution slightly differs.

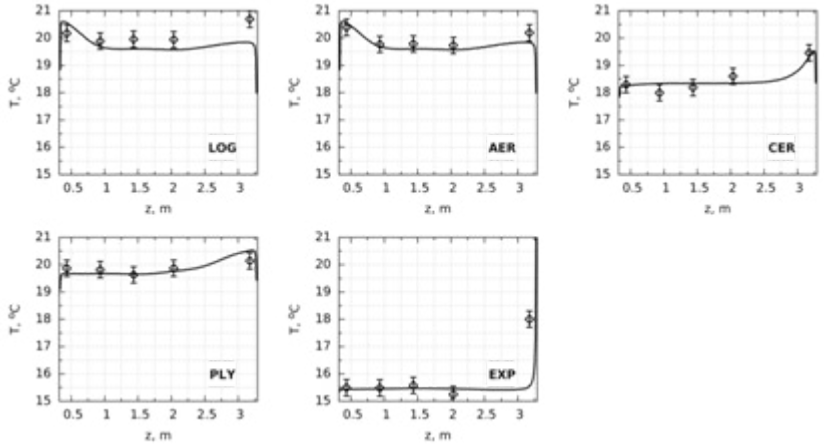

Fig. 4. Comparison of the calculated vertical temperature distributions in the centre of building (solid lines) with experiment (points).

In general, both the qualitative and quantitative tendencies are well-captured by the numerical simulations. The captured tendencies are higher temperature at the floor for the (aa1) case and higher temperatures at the ceiling for (wa1) and (el1) cases. The calculation results agree with the experiments within the measurement accuracy, except for the uppermost point in EXP. The capillary heating mat on the ceiling in EXP stand consists of thin capillaries and occupies a certain installation height, which is not considered in the modelling.

5.2.6. Radiant Temperature Asymmetry

As the numerical model considers the heat exchange by radiation, the radiant temperature, which is important for the thermal comfort, can be calculated. *Figure 5* shows the vertical distribution of the radiant temperature asymmetries ΔMRT_{ud} and ΔMRT_{fb} 0.5 m from the window. Only five cases are depicted since there are small differences between (aa1) and (aa2), (el1) and (el2) and between (wa1) and (wa2).

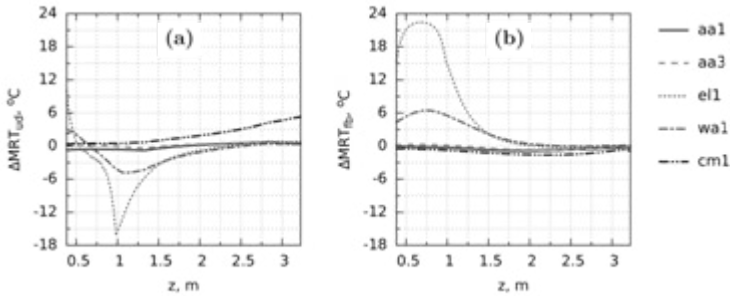

Fig. 5. Vertical distributions of radiant temperature asymmetry 0.5 m from the window (a) ΔMRT_{ud} between up and down (+z and –z); (b) ΔMRT_{fb} between front and back (+x and –x).

The inflow velocity for (aa1) is sufficiently strong to reach the floor and heat it, resulting in $\Delta MRT_{ud} < 0$ in the lower part of the room. For (aa3), the temperature of the ceiling is higher than that of the floor; therefore, $\Delta MRT_{ud} > 0$.

For the (el1) system, the distributions are strongly affected by the high-temperature heater. The maximum vertical asymmetry is observed at its upper z coordinate of 98.4 cm. Face to bottom asymmetry $\Delta MRT_{fb} > 0$ since the heater is located in the +x direction, and it reaches about 22 °C in the vicinity of the heater.

The qualitative behaviour of the (wa1) case is similar to (el1). The maximum of vertical asymmetry is observed at the upper z coordinate of the heater of 105 cm.

5.2.7. Thermal Comfort

The thermal comfort is analysed based on the standard ISO 7730:2005 [4]. For the highest category A thermal environment the restrictions are drought rate DR < 10 %, vertical air temperature difference Percentage Dissatisfied (PD) < 3 %, warm or cool floor PD < 10 %, and radiant asymmetry PD < 5 %. These values are recalculated to maximum allowable flow velocity and temperature difference using formulas from [4] under consideration of clothing and activity level.

For the local temperature of 23 °C, the condition for the draught rate DR < 10 % yields the maximum velocity of 0.18 m/s. Analysing the calculated velocity fields (see *Fig. 3*, isoline of 0.2 m/s), it is concluded that the inflow velocity of the air-air heat pump (or ventilation device) is sufficiently high and the thermal comfort conditions regarding the draught rate are not satisfied in small-size test stands.

The condition PD < 3 % for the vertical air temperature difference between the head and ankles corresponds to the maximum temperature difference of 2.7 °C or 6 temperature isolines in *Fig. 3*. All the considered cases except aa3 satisfy this comfort condition since the temperature differences do not exceed 1.5 °C.

The condition PD < 10 % for the warm or cool floor corresponds to the floor temperature in the range of 19.2–28.0 °C. By analysing the average floor temperatures in *Table 1*, it is concluded that this condition is satisfied only for the cases with the highest heating power – wa1 and wa2. The experimental target temperature of 20 °C was 2 °C lower than the optimum operative temperature of 22°C in A class buildings [4]. If the temperature is increased by 2 °C by increasing the heating power, the cold floor condition will not be satisfied only for cases (cm1) and (aa3).

The condition PD < 5 % for the radiant temperature asymmetry corresponds to the maximum radiant temperature asymmetry of 4.0 °C for warm ceiling and 25.8 °C for warm wall. For (el1), (el2) and (cm1) the condition for a warm ceiling is not satisfied.

6. CONCLUSIONS

It has been demonstrated that the numerical modelling is a valuable tool, which supplements experimental measurements and allows gaining more insight into heat and mass transfer and thermal comfort in rooms. The developed mathematical model has been validated by comparing the temperature distributions in the middle of the room for four different experimental setups, and rather good agreement with experiment is achieved.

The air-air heat pump system produces the highest mean air temperature per applied thermal heating power, followed by air-water heat pump, electrical heater and capillary ceiling mat.

The thermal comfort cannot be satisfied with respect to the draught rate if the air-air heat pump is used for ventilation in the considered small-size test stands. For the vertical air temperature difference between the head and ankles, the comfort conditions are satisfied when using air-air heat pump in ventilation mode together with any other heating system. The comfort regarding cool floor can be satisfied by increasing the heating power, but the air-air heat pump with slow inflow velocity and ceiling mat are unfavourable solutions. The discomfort of radiant temperature asymmetry is observed in case of capillary heating mat and close to the electric heater.

ACKNOWLEDGEMENTS

The present research has been supported by the European Social Fund; the project is implemented by the University of Latvia, No. 2013/0027/1DP/1.1.1.2.0/13/APIA/VIAA/007.

REFERENCES

1. Rhee, K.N., Kim, K.W. (2015). A 50 year review of basic and applied research in radiant heating and cooling systems for the built environment. *Building and Environment 91*, 166–190.
2. Hakkaki-Fard, A., Eslami-Nejad, P. Aidoun, Z., and Ouzzane, M. (2015). A techno-economic comparison of a direct expansion ground-source and an air-source heat pump system in Canadian cold climates. *Energy 87* (1), 49–59.
3. Garcia, J.A. (2010). A Review of General and Local Thermal Comfort Models for Controlling Indoor Ambiences. *Air Quality*, Ashok Kumar (Ed.), ISBN: 978-953-307-131-2, InTech.
4. ISO 7730:2005. (2005). *Ergonomics of the Thermal Environment – Analytical Determination and Interpretation of Thermal Comfort Using Calculation of the PMV and PPD Indices and Local Thermal Comfort Criteria.* Geneva, Switzerland: International Organization for Standardization.
5. Myhren, J.A., and Holmberg S. (2008). Flow patterns and thermal comfort in a room with panel, floor and wall heating. *Energy and Buildings 40* (4), 524–536.
6. Stamou, A., and Katsiris, I. (2006). Verification of a CFD model for indoor airflow and heat transfer. *Building and Environment 41* (9), 1171–1181.
7. Tiberiu C., Virgone, J., and Kuznik, F. (2009). Evaluation of thermal comfort using combined CFD and experimentation study in a test room equipped with a cooling ceiling. *Building and Environment 44* (8), 1740–1750.
8. Jakovics, A., Gendelis, S., Ratnieks, J., and Sakipova, S. (2014). Monitoring and Modelling of Energy Efficiency for Low Energy Testing Houses in Latvian Climate Conditions. *International Journal of Energy. 8*, 76–83.
9. Greitans, M., Grunde, U., Jakovics, A., and Gendelis, S. (2013). Web-based real-time data acquisition system as tool for energy efficiency monitoring. In: 21st Telecommunications Forum (TELFOR), 26–28 November 2013 (pp. 553–556). Belgrade, Serbia: IEEE.

10. Datasheet SHT7x Humidity and Temperature Sensor IC. (2015). Available at http://www.sensirion.com/fileadmin/user_upload/customers/sensirion/Dokumente/Humidity/Sensirion_Humidity_SHT7x_Datasheet_V5.pdf.
11. The Open Source CFD Toolbox OpenFOAM. (2015). Available at http://www.openfoam.org/
12. Langley Research Center Turbulence Modelling Resource. (2015). Available at http://turbmodels.larc.nasa.gov/sst.html.
13. Menter, F. R., Kuntz, M., and Langtry, R. (2003). Ten Years of Industrial Experience with the SST Turbulence Model. *Turbulence, Heat and Mass Transfer. 4*, 625–632.
14. Ratnieks, J., Jakovičs, A., and Gendelis, S. (2014). Mathematical modelling of airflow velocity and temperature fields for experimental test houses. In: Proceedings of the 10th Nordic Symposium on Building Physics, 15–19 June 2014, (pp. 871–878). Lund, Sweden.

GAISA PLŪSMAS, SILTUMA PĀRNESES UN TERMISKĀ KOMFORTA EKSPERIMENTĀLA UN SKAITLISKA ANALĪZE ĒKĀS AR DAŽĀDĀM APKURES SISTĒMĀM

A. Sabanskis, J. Virbulis

K o p s a v i l k u m s

Temperatūras, mitruma un gaisa plūsmas monitorings veikts 5 eksperimentālās ēkās ar iekšējiem izmēriem 3x3x3 m^3, kas atrodas Rīgā, Latvijā. Ēkas ir aprīkotas ar dažādām apkures sistēmām, tādām kā gaiss-gaiss siltumsūknis, gaiss-ūdens siltumsūknis, griestu kapilārais sildīšanas paklājs un elektriskais sildītājs. Gaisa plūsmas un siltuma pārneses konvekcijas, vadīšanas un starojuma ceļā skaitliska modelēšana veikta izmantojot OpenFOAM programmatūru un iegūtie rezultāti salīdzināti ar eksperimentāliem datiem. Rezultāti tiek analizēti attiecībā uz temperatūras un gaisa plūsmas sadalījumiem kā arī termisko komfortu.

28.07.2015.

LATVIAN JOURNAL OF PHYSICS AND TECHNICAL SCIENCES
2016, N 2

DOI: 10.1515/lpts-2016-0011

SOLID STATE PHYSICS

STUDY OF COPPER NITRIDE THIN FILM STRUCTURE

A. Kuzmin, A. Kalinko, A. Anspoks, J. Timoshenko, R. Kalendarev

Institute of Solid State Physics, University of Latvia,
8 Kengaraga Str., Riga, LV-1063, LATVIA
e-mail: a.kuzmin@cfi.lu.lv

X-ray diffraction and x-ray absorption spectroscopy at the Cu K-edge were used to study the atomic structure in copper nitride (Cu_3N) thin films. Textured nanocrystalline films are obtained upon dc magnetron sputtering on substrates heated at about 190 °C, whereas amorphous films having strongly disordered structure already in the second coordination shell of copper are deposited in the absence of heating.

Keywords*: copper nitride, thin film, x-ray diffraction, x-ray absorption spectroscopy.*

1. INTRODUCTION

Copper nitride (Cu_3N) has a cubic anti-ReO_3-type structure (Fig. 1) with the lattice parameter a_0=3.811-3.820 Å and is composed of the NCu_6 octahedra joined by corners [1], [2]. Practical interest in the fabrication of copper nitride has grown in the recent years motivated by its possible applications in the thin film form as a material for write-once read many (WORM) optical storage devices [3], [4], for the fabrication of low-resistance magnetic tunnel junctions for non-volatile magnetic random access memories [5], as promising cathodic electrocatalysts in alkaline fuel cells [6], in optical lithography for fabrication of microscopic metal links [7], [8] and, very recently, as an absorber for photovoltaic and photoelectrochemical solar cells [9], [10].

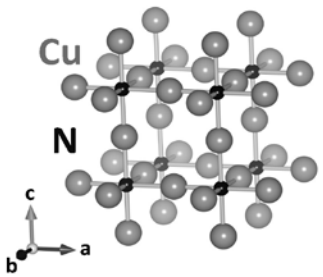

Fig. 1. Crystal structure of cubic (space group *Pm*-3*m*) antiperovskite Cu_3N built up from NCu_6 regular octahedra. Large balls are copper atoms, small balls are nitrogen atoms.

The atomic structure of Cu_3N facilitates anisotropic thermal vibrations of Cu atoms, whose thermal ellipsoids are flattened in the direction perpendicular to the N–Cu–N atomic chains [1], and accepts the presence of nitrogen vacancies or nitrogen/copper interstitial dopants that may result in a variation of the lattice parameter by up to ±0.08 Å [11], [12].

Chemical bonding and electronic properties of Cu_3N are strongly related to its atomic structure. The Cu–N bonds along linear N–Cu–N atomic chains are partially covalent due to an admixture of Cu(4s, 4p) states to the Cu(3d)-N(2p) bands, which do not lead to a covalent energy gain alone [13]. Cu_3N is a narrow band gap (0.25–1.90 eV [10]) semiconductor. However, small changes in the interactions between copper atoms stimulated by the formation of nitrogen vacancies may result in further band gap narrowing or even band overlap [11], because the nearest Cu–Cu distance of about 2.70 Å in Cu_3N is only slightly larger than that of 2.56 Å found in metallic copper. The transition of Cu_3N to metallic state can also be promoted by copper doping [14], [15] or by applying high pressure [16], [17]. Thus, the information on the local atomic structure and disorder in Cu_3N thin films is important for the understanding and tuning of their properties.

In this study, we have performed complementary x-ray diffraction and x-ray absorption spectroscopy investigations of the atomic structure in Cu_3N thin films produced by dc magnetron sputtering as a function of film preparation conditions.

2. EXPERIMENTAL AND DATA ANALYSIS

Polycrystalline Cu_3N thin films were prepared by dc magnetron sputtering of metal copper target in pure N_2 atmosphere on glass and polyimide substrates with average deposition rate of 2.0 nm/sec using modified magnetron sputter deposition system UVN-3. The deposition parameters and thickness of the films are reported in Table 1. The film thickness was measured by profilometer Veeco Dektak 150. Polycrystalline Cu_3N (99.5% purity, AlfaAesar) was used for comparison.

X-ray powder diffraction (XRD) patterns (Fig. 2) were recorded at room temperature (20 °C) using a θ-θ Bragg-Brentano powder diffractometer PANalytical X'Pert Pro MPD, equipped with copper anode x-ray tube (Model PW3373, Cu K_α radiation, λ=0.154 nm).

X-ray absorption measurements were performed at the Cu K-edge (8979 eV) in transmission mode at the HASYLAB/DESY C bending-magnet beamline [18] at room temperature. The storage ring DORIS III operated at E=4.44 GeV and I_{max}=140 mA. The higher order harmonics were reduced by detuning the double-monochromator Si(111) crystals to 60 % of the rocking curve maximum, using the beam-stabilization feedback control. The x-ray beam intensity was measured by ionization chambers filled with argon and krypton gases.

X-ray absorption spectra were analysed using the EDA software package [19]. The extended X-ray absorption fine structure (EXAFS) $\chi(k)$ was isolated following a conventional procedure [20], [21]. The contribution from the first (Cu–N) and second (Cu–Cu) coordination shells was singled out using Fourier filtering procedure in the range of 0.8–3.1 Å and analysed within the single-scattering Gaussian approxi-

mation to determine structural parameters. The self-consistent, real space multiple-scattering FEFF8.2 code [22], [23] was used to generate the backscattering amplitude and phase shift functions for Cu–N and Cu–Cu atom pairs based on crystallographic data of Cu_3N [1]. The complex exchange-correlation Hedin-Lundqvist potential was used to account for inelastic effects. The crystal potential was of muffin-tin (MT) type, and the values of the MT-radii were R_{MT}(Cu)=1.22 Å and R_{MT}(N)=0.97 Å.

Table 1

Thin Film Preparation Conditions, Thickness and Lattice Parameter of Cu_3N Samples

Sample	Deposition time (sec)	Substrate temperature (°C)	Film thickness (nm)	Lattice parameter (Å)
Bulk Cu_3N	-	-	-	3.819
TF1	120	20	229	-
TF2	30	191	74	3.816
TF3	120	196	224	3.796

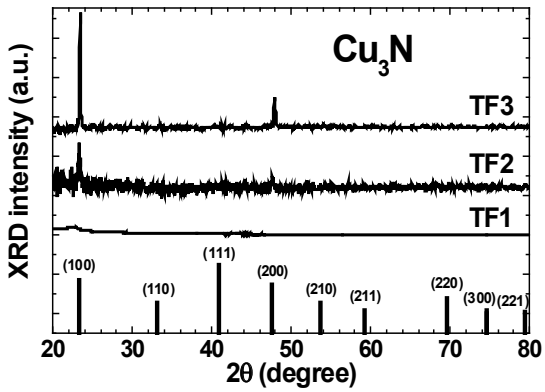

Fig. 2. X-ray diffraction patterns for Cu_3N thin films. Vertical bars show positions of the Bragg peaks for bulk Cu_3N phase (JCPDS No. 47-1088).

3. RESULTS AND DISCUSSION

The thin film TF1 deposited at the substrate temperature of 20 °C is amorphous (Fig. 2), and its XRD pattern originated mainly from the glass substrate. Two other films deposited at the substrate temperatures of 191 °C (TF2) and 196 °C (TF3) are nanocrystalline and strongly textured with crystal growth direction [100]. Their diffraction patterns are indexed to the (100) and (200) planes of cubic Cu_3N. Note that similar preferential growth of Cu_3N along the [100] direction was reported in [11], [24], [25] for films produced by reactive radio-frequency (RF) magnetron sputtering. The lattice parameter a_0 in thin film samples TF2 and TF3 determined from the position of the (100) and (200) peaks is slightly smaller than in bulk Cu_3N (Table 1) that indicates some substoichiometry of the films [11].

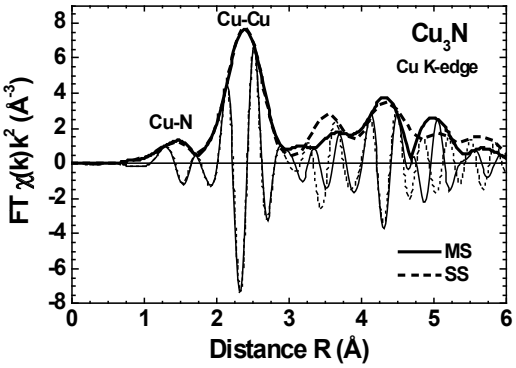

Fig. 3. Fourier transforms (thin lines – imaginary parts and thick lines – moduli) of the calculated Cu K-edge EXAFS $\chi(k)k^2$ for Cu_3N. Solid line – the signal including all multiple-scattering (MS) contributions up to the 6th order, dashed line – the signal including only the single-scattering (SS) contributions. Note that the positions of the peaks differ from the crystallographic values due to the phase shift present in EXAFS.

Table 2

Interatomic Distances (*R*, ±0.01 Å) and Mean-Squared Relative Displacements (σ^2, ±0.0007 Å^2) for Nearest Cu–N and Cu–Cu Atom Pairs Obtained from the Analysis of the Cu K-edge EXAFS Spectra

Sample	Cu–N		Cu–Cu	
	R (Å)	σ^2 (Å^2)	*R* (Å)	σ^2 (Å^2)
Bulk Cu_3N	1.89	0.0022	2.64	0.0130
TF1	1.88	0.0022	2.60	0.0270
TF2	1.90	0.0024	2.67	0.0184
TF3	1.89	0.0026	2.68	0.0158

Since Cu_3N has anti-perovskite type structure with linear Cu–N–Cu atomic chains, one can expect significant contribution of the multiple-scattering (MS) effects [26] into EXAFS. Therefore, we have performed ab initio multiple-scattering calculations by the FEFF8.2 code [22], [23] for bulk Cu_3N to estimate the *R*-space range where such contributions are important. No thermal effects were included into calculations, leading to overestimated peak amplitudes. The obtained results are reported in Fig. 3 and suggest that the first two peaks in Fourier transform (FT) of EXAFS, which correspond to the first (Cu–N atom pair) and second (Cu–Cu atom pair) coordination shells of copper, are free from MS contributions and, thus, can be analysed within the single-scattering (SS) approximation using conventional multicomponent analysis procedure [20], [21]. The analysis of peaks above 3 Å requires inclusion of the MS effects through some sophisticated procedure, as, for example, described in [27], and will not be discussed here.

The shape of the Cu K-edge EXAFS for the films TF2 and TF3 produced on heated substrates is close to that in bulk Cu_3N, except some features are less resolved (Fig. 4). A comparison of their Fourier transforms suggests the nanocrystalline structure of the films appearing as progressive reduction of the amplitude of distant peaks due to a contribution of under-coordinated atoms located at the nanocrystallite surface. The high frequency contributions from the outer coordination shells are dra-

matically reduced in EXAFS of the film TF1 deposited on unheated substrate that reflects disappearance of the long-range order in the film, in agreement with XRD data (Fig. 2).

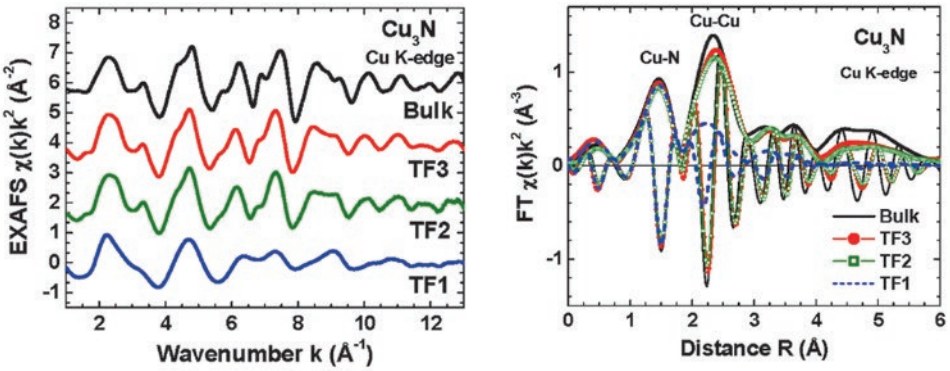

Fig. 4. Experimental Cu K-edge EXAFS $\chi(k)k^2$ and their Fourier transforms (both imaginary parts and moduli are shown) for bulk Cu_3N and thin films.

The values of structural parameters (interatomic distances R and mean-squared relative displacements (MSRD) σ^2) obtained from the analysis of the first two peaks in FTs are reported in Table 2 for bulk Cu_3N and thin films. Note that the coordination numbers (N=2 for Cu–N and N=8 for Cu–Cu) in the films remain as in the bulk within the error of the fit. Also the length of the Cu–N bonds and the MSRD values in all films are close to those in bulk Cu_3N. Moreover, rather small values of the Cu–N MSRDs indicate strong bonding through a mixing of Cu(4s, 4p) states with the Cu(3d)-N(2p) bands estimated by the first principles of electronic structure calculations in [13]. The intensity of the second peak due to the Cu–Cu bonds is reduced in the films due to increasing disorder as is evidenced by the MSRD, whose value increases nearly twice in the amorphous film TF1 compared to bulk Cu_3N.

4. CONCLUSIONS

The atomic structure of copper nitride thin films produced by dc magnetron sputtering was studied by x-ray diffraction and x-ray absorption spectroscopy at the Cu K-edge. We found that the nearest interatomic distance Cu–N in thin films did not change significantly upon substrate heating and was close to that in bulk Cu_3N, indicating strong bonding between copper and nitrogen atoms. At the same time, the second Cu–Cu and outer coordination shells were strongly influenced by structural disorder, which could be reduced by substrate heating during film deposition.

ACKNOWLEDGEMENTS

The present research has been supported by the Latvian National Research Program IMIS2. The EXAFS measurements have been financed from the European Community's Seventh Framework Programme under grant agreement No. 226716 (Project I-20100098 EC).

REFERENCES

1. Zachwieja, U., and Jacobs, H. (1990). Ammonothermalsynthese von kupfernitrid, Cu_3N. *J. Less Common Metals 161*, 175–184. DOI: 10.1016/0022-5088(90)90327-G.
2. Paniconi, G., Stoeva, Z., Doberstein, H., Smith, R. I., Gallagher, B. L., and Gregory, D.H. (2007). Structural chemistry of Cu_3N powders obtained by ammonolysis reactions. *Solid State Sci.* ***9***, 907–913. DOI: 10.1016/j.solidstatesciences.2007.03.017.
3. Asano, M., Umeda, K., and Tasaki, A. (1990). Cu_3N thin film for a new light recording media. *Jpn. J. Appl. Phys. 29*, 1985–1986. DOI: 10.1143/JJAP.29.1985.
4. Maruyama, T., and Morishita, T. (1996). Copper nitride and tin nitride thin films for write-once optical recording media. *Appl. Phys. Lett. 69*, 890–891. DOI: 10.1063/1.117978.
5. Borsa, D.M., Grachev, S., Presura, C., and Boerma, D.O. (2002). Growth and properties of Cu_3N films and Cu_3N/γ'-Fe_4N bilayers. *Appl. Phys. Lett. 80*, 1823–1825. DOI: 10.1063/1.1459116.
6. Wu, H., and Chen, W. (2011). Copper nitride nanocubes: size-controlled synthesis and application as cathode catalyst in alkaline fuel cells. *J. Am. Chem. Soc. 133*, 15236–15239. DOI: 10.1021/ja204748u.
7. Maya, L. (1993). Deposition of crystalline binary nitride films of tin, copper, and nickel by reactive sputtering. *J. Vac. Sci. Technol. A 11*, 604–608. DOI: 10.1116/1.578778.
8. Borsa, D.M., and Boerma, D.O. (2004). Growth, structural and optical properties of Cu_3N films. *Surf. Sci. 548*, 95–105. DOI: 10.1016/j.susc.2003.10.053.
9. Zakutayev, A., Caskey, Ch.M., Fioretti, A.N., Ginley, D.S., Vidal, J., Stevanovic, V., Tea, E., and Lany, S. (2014). Defect tolerant semiconductors for solar energy conversion. *J. Phys. Chem. Lett. 5*, 1117–1125. DOI: 10.1021/jz5001787.
10. Caskey, Ch. M., Richards, R.M., Ginleya, D.S., and Zakutayev, A. (2014). Thin film synthesis and properties of copper nitride, a metastable semiconductor. *Mater. Horiz. 1*, 424–430. DOI: 10.1039/c4mh00049h.
11. Pierson, J.F. (2002). Structure and properties of copper nitride films formed by reactive magnetron sputtering. *Vacuum 66*, 59–64. DOI: 10.1016/S0042-207X(01)00425-0.
12. Maruyama, T., and Morishita, T. (1995). Copper nitride thin films prepared by radio-frequency reactive sputtering. *J. Appl. Phys. 78*, 4104–4107. DOI: 10.1063/1.359868.
13. Hahn, U., and Weber, W. (1996). Electronic structure and chemical-bonding mechanism of Cu_3N, Cu_3NPd, and related Cu(I) compounds. *Phys. Rev. B* ***53***, 12684. DOI: 10.1103/PhysRevB.53.12684.
14. Moreno-Armenta, M.G., Martínez-Ruiz, A., and Takeuchi, N. (2004). Ab initio total energy calculations of copper nitride: The effect of lattice parameters and Cu content in the electronic properties. *Solid State Sci.* 6, 9–14. DOI: 10.1016/j.solidstatesciences.2003.10.014.
15. Hou, Z.F. (2008). Effects of Cu, N, and Li intercalation on the structural stability and electronic structure of cubic Cu_3N. *Solid State Sci.* 10, 1651–1657. DOI: 10.1016/j.solidstatesciences.2008.02.013.
16. Zhao, J.G., Yang, L.X., and Yu, Y., (2006). Pressure-induced metallization and structural evolution of Cu_3N. *Phys. Stat. Sol. (b)* 243, 573–578. DOI: 10.1002/pssb.200541280.
17. Wosylus, A., Schwarz, U., Akselrud, L., Tucker, M.G., Hanfland, M., Rabia, K., Kuntscher, C., von Appen, J., Dronskowski, R., Rau, D., and Niewa, R. (2009). High-pressure phase transition and properties of Cu_3N: An experimental and theoretical study. *Z. Anorg. Allg. Chem.* 635, 1959–1968. DOI: 10.1002/zaac.200900369.

18. Rickers, K., Drube, W., Schulte-Schrepping, H., Welter, E., Brüggmann, U., Herrmann, M., Heuer, J., and Schulz-Ritter, H. (2007). New XAFS Facility for In-Situ Measurements at Beamline C at HASYLAB. A*IP Conf. Proc. 882*, 905–907. DOI: 10.1063/1.2644700
19. Kuzmin, A. (1995). EDA: EXAFS data analysis software package. *Physica B 208-209*, 175–176. DOI: 10.1016/0921-4526(94)00663-G.
20. Aksenov, V.L., Kuzmin, A.Yu., Purans, J., and Tyutyunnikov, S.I. (2006). Development of Methods of EXAFS Spectroscopy on Synchrotron Radiation Beams: Review. *Crystallogr. Rep. 51*, 908–935. DOI: 10.1134/S1063774506060022.
21. Kuzmin, A., and Chaboy, J. (2014). EXAFS and XANES analysis of oxides at the nanoscale. *IUCrJ 1*, 571–589. DOI: 10.1107/S2052252514021101.
22. Ankudinov, A.L., Ravel, B., Rehr, J.J., and Conradson, S.D. (1998). Real-space multiple-scattering calculation and interpretation of x-ray-absorption near-edge structure. *Phys. Rev. B 58*, 7565–7576. DOI: 10.1103/PhysRevB.58.7565.
23. Rehr, J.J., and Albers, R.C. (2000). Theoretical approaches to x-ray absorption fine structure. *Rev. Mod. Phys.* 72, 621–654. DOI: 10.1103/RevModPhys.72.621.
24. Xiao, J., Li, Y., and Jiang, A. (2011). Structure, optical property and thermal stability of copper nitride films prepared by reactive radio frequency magnetron sputtering. *J. Mater. Sci. Technol. 27*, 403–407. DOI: 10.1016/S1005-0302(11)60082-0.
25. Yue, G.H., Yana, P.X., and Wang, J. (2005). Study on the preparation and properties of copper nitride thin films. *J. Crystal Growth 274*, 464–468. DOI: 10.1016/j.jcrysgro.2004.10.032.
26. Kuzmin, A., and Purans, J. (1993). A new fast spherical approximation for calculation of multiple scattering contribution in the X-ray absorption fine structure and its application to ReO_3, $NaWO_3$ and MoO_3. *J. Phys.: Condensed Matter 5*, 267–282. DOI: 10.1088/0953-8984/5/3/004.
27. Anspoks, A., Kalinko, A., Kalendarev, R., and Kuzmin, A. (2012). Atomic structure relaxation in nanocrystalline NiO studied by EXAFS spectroscopy: Role of nickel vacancies. *Phys. Rev. B 86*, 174114, 1–11. DOI: 10.1103/PhysRevB.86.174114.

VARA NITRĪDA PLĀNO KĀRTIŅU STRUKTŪRAS PĒTĪJUMI

A. Kuzmins, A. Kalinko, A. Anspoks,
J. Timošenko, R. Kalendarev

K o p s a v i l k u m s

Šajā darbā mēs ziņojam par vara nitrīda (Cu_3N) plāno kārtiņu rentgendifrakcijas un rentgenabsorbcijas spektroskopijas pētījumu rezultātiem. Teksturētas nanokristāliskās plānās kartiņas tika iegūtas, izmantojot līdzstrāvas magnetrona izputināšanas procesu uz pamatnēm, kas karsētas ap 190°C temperatūrā. Amorfas plānās kārtiņas ar stipri nesakārtotu struktūru jau vara otrajā koordinācijas sfērā tika sagatavotas bez pamatnes karsēšanas.

05.11.2015.

LATVIAN JOURNAL OF PHYSICS AND TECHNICAL SCIENCES
2016, N 2

DOI: 10.1515/lpts-2016-0012

DEVELOPMENT OF MATHEMATICAL MODELS FOR DETECTING MICRON SCALE VOLUMETRIC DEFECTS IN THIN FILM COATINGS

G. Gaigals, M. Donerblics, G. Dreifogels

Ventspils University College,
101 Inženieru Str., Ventspils, LV-3601, LATVIA
gatis.gaigals@venta.lv

The focus of the present research is to investigate possibilities of volumetric defect detection in thin film coatings on glass substrates by means of high definition imaging with no complex optical systems, such as lenses, and to determine development and construction feasibility of a defectoscope employing the investigated methods. Numerical simulations were used to test the proposed methods. Three theoretical models providing various degrees of accuracy and feasibility were studied.

Keywords: *deconvolution, compressive sampling,* ℓ_1 *minimization, numeric simulation, thin film coatings*.

1. INTRODUCTION

To assess the quality and usability of a glass substrate covered with thin film coating it is of utmost importance to detect positions of volumetric defects, if any present, in said coatings. To do this rapidly, in manufacturing setting an automated process for detecting micron scale volumetric defects is necessary. Mechanically, the following process can be proposed: the sample (glass substrate covered with thin film coating) is fed (by a conveyer) to a test station where one side of the sample is uniformly illuminated. A sensor of some sort is positioned on the other side of the sample. If no defects are present – the sensor should produce a uniform reading. If a defect is present in the sample, it should produce a non-uniform reading from the sensor, which shall allow for determination of a defect position. In this paper, three methods for detecting position of micron scale volumetric defects, two using a one-pixel camera as a sensor and one using a pixel matrix, are proposed and tested by means of numeric simulation.

2. THEORETICAL BASIS

Convolution. In imaging, if no optical devices, such as lenses, are used, the result sampled from a sensor can be viewed as convolution between function $f(x)$,

which describes intensity of light reflected off or emitted from the object being photographed, and the visibility function $g(x)$, set by parameters of the sensor (pixel). The continuous time convolution (mathematically marked as operator) of two functions $f(x)$ and $g(x)$ in one-dimensional (1D) case is an integral, when function $g(x)$ is mirrored and shifted over $f(x)$ [1]. Often the integral is taken over infinite time; however, for real world applications finite time variation is used:

$$f(x) * g(x) = \int_0^t f(y)\, g(x-y)dy. \tag{1}$$

In two-dimensional (2D) occasion, discrete convolution (operator $\otimes$) is given by formula:

$$f(x,y) \otimes g(x,y) = \sum_{s=-a}^{a} \sum_{t=-b}^{b} f(s,t)g(x-s, y-t). \tag{2}$$

In signal processing, convolution also describes the multiplication of spectra from two signals [2]. The definition of convolution suggests that the opposite – the reconstruction of one of the initial functions is possible if the other function and the convolution are known. Such a procedure is called deconvolution [3]. In other words, deconvolution is the inverse mathematical operation of convolution:

$$(f * g) + \epsilon = h, \tag{3}$$

where *h* is the resulting signal, *f* – the renewable signal, *g* – the interference signal, but describes noise. Deconvolution can also be achieved by dividing the convolution spectrum by spectrum of the known initial function. This in turn produces spectrum of the other initial function, which can be transformed to time domain [1], [2].

Compressive sampling (compressed sensing, CS) is a signal sampling technique that allows representing a compressible signal $f(x)$ as signal $y(x)$ with sample count *n* and *m* respectively by use of easily implementable expression

$$y(x) = Af(x), \tag{4}$$

where *A* is the so-called measurement matrix, but $y(x)$ is a measurement. As a result, $m \ll n$. For recovery of signal $f(x)$ ℓ_1 -minimisation algorithms must be used [4].

To exploit CS, the measurement matrix A must conform to specific rules and ensure specific properties [5]. The most important is the coherence property of the measurement matrix A that determines how many elements measurement $y(x)$ should contain to allow for perfect recovery of $f(x)$.

3. PROPOSED METHODS

Based on the theory, three methods for detecting the positions of volumetric defects in thin film coatings on a given glass sample were proposed.

The first method utilises a direct algorithm of convolution, where function f represents normalized translucency of the sample but function g represents normalized visibility function of the sensor. This model uses a one-pixel sensor for detection of light passing through the sample. For ease of mathematics, a cosine was chosen to represent the sensor visibility function.

The mechanics of this model is as follows: the sensor is set at known distance h from the sample and the sensor viewing angle α is known.

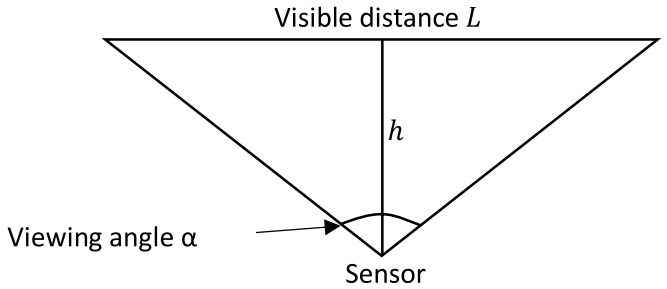

Fig. 1. Schematic of visibility distance calculation.

Mathematically, the visible distance L is calculated by equation

$$L = 2\sqrt{\left(\frac{h}{Sin\left(\frac{\alpha}{2}\right)}\right)^2 - h^2}. \tag{5}$$

In Fig. 1 the line L representing the visible distance can be imagined as a conveyor. In the mathematical model, it is realized by a one-dimensional array with length L, which represents the sample translucency function $f(L)$. Initially, all elements are set to one, representing a fully translucent medium with no sample present. Next the viewing angle alpha is expressed in radians and used in cosine calculations to construct the visibility function $g(L)$. When the measurement process starts, iteratively the convolution of functions $f(L)$ and $g(L)$ is calculated, thus simulating a conveyor to move the sample precisely by one unit (size of defect). If there are no more sample coefficients available, the first value of $f(L)$ is set to one, thus representing a situation where the sample is about to pass the sensor. This way, for the last iteration $f(L)$ is uniformly equal to one, therefore returning to the initial state.

To detect the position of a volumetric defect it is necessary to calibrate the system. This is done by simulating a result from a sample with no defects. The calibrated measurement is compared to the measurement of the sample by subtracting them. The position of the first nonzero element represents the position of a volumetric defect in the sample. This algorithm of position detection works only to find the position of the first defect. This is not suitable if all defects need to be accounted for; however, this method is applied for such purposes. The key is to recalculate calibration each time a defect is found by introducing the said defect in the calibrated measurement.

The second method is based on the Fast Fourier Transform (FFT) and spec-

trum properties of convolution. The experimental setup is the same as for the first method, to produce convolution, which corresponds to a measurement. To recover the original $f(L)$ function, spectrum of the measurement must be divided by spectrum of $f(L)$, and transformed to time domain by inverse FFT. By doing this, the translucency function of the sample within a visibility range is recovered. By repeating this process iteratively and recording results in order, it is possible to reconstruct the whole sample. Moreover, this method is easily performable in two-dimensional (2D) setting. To do this the visibility function must be expanded in 2D, representing a surface of a cosine and the "conveyor" system must be changed so that the sample is moved in 2D through the visibility range.

The third method. In a 1D case of the third method, convolution of a given signal $f(x)$ with convolution kernel $g(x)$ variously shifted in time can be implemented by using (4) so that signal $f(x)$ can be reconstructed by the method used in compressed sensing: ℓ_1-minimisation. The third method uses similar mechanical setup as described previously; however, a multiple pixel sensor is used and during measurement, the conveyor is stationary, since there is no need to shift the sample. It is assumed that all pixels have a similar visibility function that is cut at both sides (1D case) of measurement system by use of black walls (see Fig. 2).

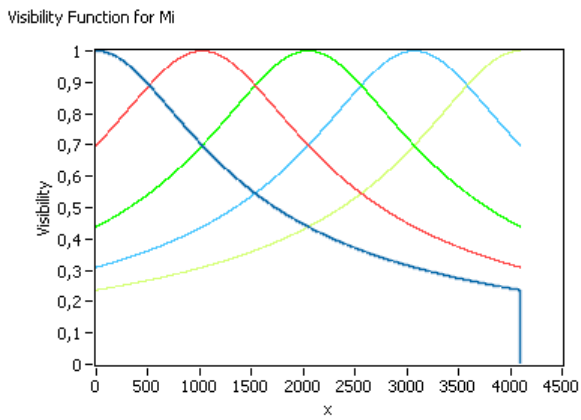

Fig. 2. Visibility function of 5 imaging pixels.

To use compressive sampling signal recovery methods, the signal has to be sparse or has to have a sparse representation [6]. Yet in a 1D case of a semi-translucent sample, the signal $f(x)$ will not be sparse. Nevertheless, the compressive sampling methods can be used if signal $f(x)$ has in time (or in this case along 1D axis) a constant value a with some (sparse) places where signal is 0. If this is the case, a sparse function $f'(x)$ can be found

$$f(x) = 1 - f'(x) \rightarrow f'(x) = a(x) - f(x), \tag{6}$$

where $a(x) = \{a, \dots, a\}$. Placing $f(x)$ in (4) will give

$$y(x) = A\big(a(x) - f'(x)\big) = Aa(x) - Af'(x). \tag{7}$$

It means that the sampled signal $y(x)$ will contain some constant aA_i in each measurement i, where A_i is row i of A. The $\sum_j A_{ij}$ can be called amplification factor of i^{th} measurement. To find $f(x)$ using (6) the sparse $f'(x)$ has to be found from

$$Aa(x) - y(x) = Af'(x). \tag{8}$$

To recover signals that are compressible but not sparse in traditional sparsifying transformations from measurements $y(x)$, the sampling system has to register the described signal value *a*. Similarly, formulas can be developed for these kinds of signals if the minimum of the signal is some constant b. Moreover, if this signal has in time (or dimension) changing value of maxima (minima) $a(x) = F(x)$, where $F(x)$ is some known function, the compressive sampling technique still can be used to sample the signal.

It follows that maximum, minimum or exact values of coated sample translucency are not important for modelling, which allows simplifying the experiment using 1 to represent translucency of a sample value without a defect and 0 for defects.

4. EXPERIMENTAL RESULTS AND DISCUSSION

For modelling, testing and simulations, the National Instruments graphical programming environment "LabVIEW" was used. Due to time and processing power constraints, simulations were limited, yet a sufficient amount of information was gathered to perform the statistical analysis.

The first method's front panel is shown in Fig. 3. For simulation and result analysis, a 100 coefficient long sample (100 μm) was used. The sensor viewing angle was swept from 1 to 160 degrees, the translucency of a defect was swept from 0 to "No defect" while the sensor distance to the sample (h) was swept from 1 to 100 units. For calculations, a numeric type "double" consisting of 64 bits was used. By analysing results, it was determined that the position of a volumetric defect was found correctly in approximately 76 % of cases; however, in the remaining 24 % of cases the position detected was ± 1 unit off. In these 24 % of cases, the resolution of calculations (64 bits) was not sufficient to detect a change in results.

To test the second method, two LabVIEW projects were created: for a one-dimensional case and for a two-dimensional case, respectively.

For simulation and result analysis, a 100 by 100 coefficient sample was used, the sensor viewing angle was swept from 1 to 160 degrees, and the sensor distance to the sample (h) was swept from 1 to 100 coefficients. From one to five randomly placed volumetric defects with varying translucency were introduced in the sample.

After data analysis an unexpected result was found; in a one-dimensional case, results, both for one and multiple volumetric defect samples, showed that the positions of the defects were found correctly (as well as the translucency values were within 1 % error margin) only in 52 % of cases. For the rest 48 % of cases, the translucency value was rapidly oscillating for every other position in the sample. However, in a two-dimensional case the spectrum multiplication method found all volumetric defects correctly and returned full translucency function within 1 % tolerance in 98.6 % of time for the case with 1 volumetric defect and 97.3 % of time

for the case with multiple volumetric defects. This indicates that there can be a bug in the algorithm for a one-dimensional case or some (small) parameter causes the algorithm to work incorrectly.

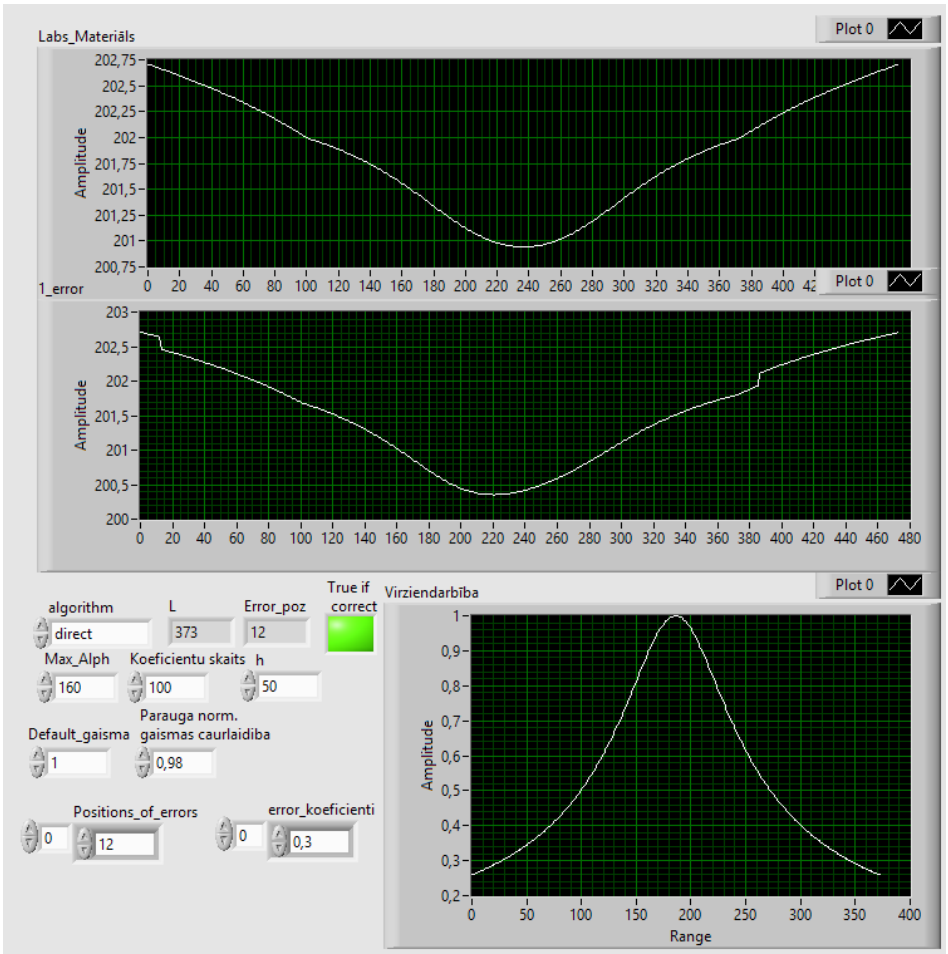

Fig. 3. Front panel example of Simple_Method.

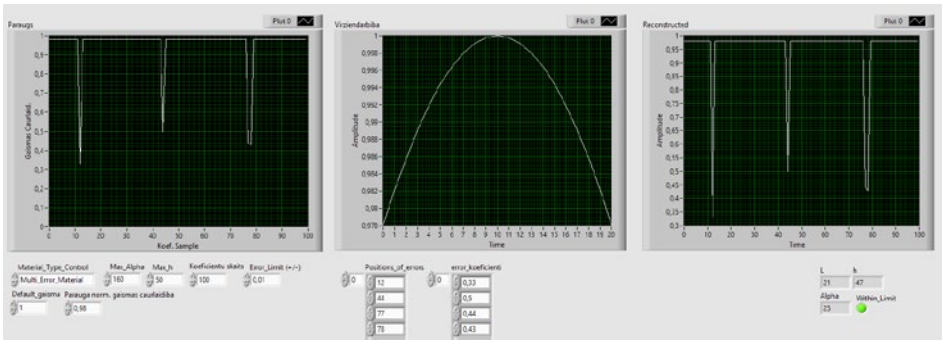

Fig. 4. Front panel of simulation using 1D FFT.

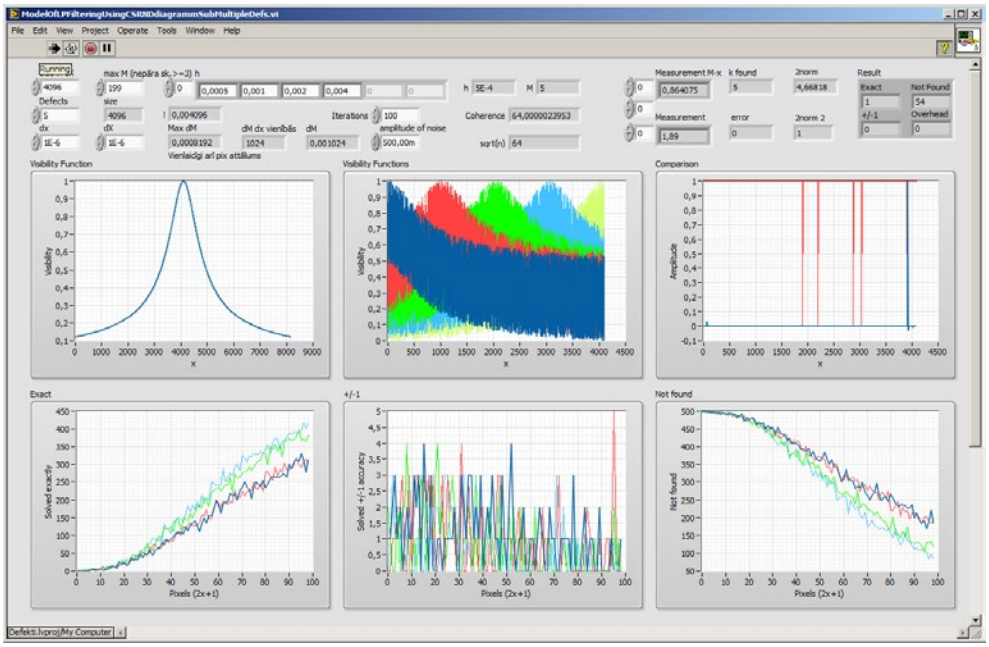

Fig. 5. Front panel of compressive sampling simulation.

The third method (see Fig. 5) was tested by using 1024 to 4096 coefficient samples possessing one to five volumetric defects with translucency value 0 set at random places for multi-error samples and all possible places in case of one defect. Sensor distance to sample (h) was swept from 0.5 mm to 1 cm. Additional simulation with $h = 10$ to 25 cm was carried out for samples with only one volumetric defect testing all possible positions of defects. This method correctly returned position of the volumetric defect in 100 % for the following defect cases: for 0.5 mm to 1 cm if the sensor had 3 to 99 pixels, for $h = 10$ cm if the sensor had less than 7 pixels (in this case, an increase in pixel count produced worse results, possibly due to error accumulation during calculations).

At first, this method failed to find multiple defects since measurement matrix A was highly coherent; therefore, each pixel visibility function was randomised (see Fig. 5 graph "Visibility Functions"), thus adding white noise (with adjustable amplitude) to the pixel visibility function (see Fig. 5 graph "Visibility Function"); afterwards the summarised visibility function was normed. Physically this means that the sensor should be illuminated through a glass with random thickness pattern. As a result, coherence of A did not improve much (see Fig 5. value "Coherence"), yet simulation was able to find multiple defects. Simulations with randomised visibility functions and 4096 unit samples produced the following results: for samples with one volumetric defect, $h \leq 25$ cm and sensor with 5 to 99 pixels the model found defect when the added random noise level was as low as 0.01 %. In case of samples with 5 volumetric defects it can be seen that an increase in pixel count and decrease in distance improve defect detection accuracy (see Fig 5. graphs "Exact", "± 1", "Not found"); results were calculated for rather unrealistic randomisation of visibility function (added noise amplitude 50 %). Additional calculations showed

that by increasing sensor pixel count the randomisation of the visibility function could be reduced.

Performance and memory. A computer with 64 bit operating system, 4 GB of RAM and Intel Pentium T4500 processor (dual core, 2.3 GHz) was used to carry out simulations. In case of the first method, it takes approximately 50 milliseconds for this system to perform a measurement, which uses, on average, 8.9 kB of memory per measurement of $100\ \mu m$ sample. In a 1D case of the second method, it takes approximately 86 milliseconds for this system to perform a measurement using, on average, 4.2 kB of memory per measurement. In a 2D case of the second method, the system uses approximately 1.7 seconds and, on average, 19.3 MB of memory per measurement. Although these numbers are significantly higher than for other cases, they are quite remarkable, since these measurements produce full translucency information of 2D visibility range. The measurement time needed for the third method is linearly dependent on a number of sensor pixels and sample defect count. In case of 99 pixels, for this system, to find one defect it takes approximately 6.1 milliseconds; however, in case of 49 pixels it takes only 3.2 milliseconds. On average, the third method uses 2.15 MB of memory per measurement.

5. FEASIBILITY OF DEFECTOSCOPE

Digital images are dependent on performance of an imaging sensor. Two widely used sensor types are CCD (Charge-Coupled Device) and COMS (Complementary Metal-Oxide-Semiconductor). Although CMOS is a newer, cheaper and more power-efficient sensor, a CCD sensor would be more appropriate for application in a defectoscope. This is so due to inherent CMOS problem called rolling shutter. The so-called rolling shutter means that the sensor is read line by line, thus skewing a moving object such as in case with a conveyor above the sensor. In case of CCD, the whole image is captured at once as well as the analogous nature of CCD can provide a higher definition if appropriate circuitry is used [7], [8].

Digital image consists of two parts – usable signal and noise, which is an integral part that arises from different sources. Three main noise sources are identified: photon noise, read-out noise and dark current noise. Listed sensor noise parameters dictate a signal-to-noise ratio (SNR). SNR value of the sensor can be determined by expression

$$SNR = \frac{PQ_e t}{\sqrt{(P+B)Q_e t + Dt + N_r^2}} \tag{9}$$

where P is photon flux, B is background photon flux (both given in photon/pixel/sec), Q_e stands for quantum efficiency of CCD, t is exposure or integration time but D is dark current. From [9], [10] it is determined that the first and second models working with 64 bit values provide an SNR value of approximately 290 dB. Best CCD sensors provide SNR up to 120 dB [6], [7] which corresponds approximately to 30 bit resolution; therefore, practical test would be necessary to determine the real life accuracy of the discussed methods. Further experiments would be necessary to

determine an SNR value provided by the third model; however, it is well known that noise has a little effect when compressive sampling is used [11].

In construction of a defectoscope that utilises the proposed methods, a precise conveyor capable of moving exactly at 1 micron intervals is needed for the first and second methods, but a precision laser measuring system must be implemented for the third method. To achieve the best possible results, the sensor must be positioned as close to the sample as possible (less than 1 mm).

6. CONCLUSIONS

All three investigated methods are capable of detecting micron scale volumetric defects in thin film coatings on glass substrates. However, each method provides different degree of accuracy and performance, thus, different potential application.

The first method is the simplest one and, potentially, the easiest to implement, since only one measurement of voltage is needed per movement of the conveyor. Yet this is also the least accurate method.

The second method needs more computing resources, however, could prove to be suitable in research setting where a full translucency analysis of the sample can be useful.

In manufacturing setting, the third method would be the most appropriate, since it is the fastest and most accurate in detecting position of one volumetric defect at quite large distances (up to 25 cm) as well as it needs a simple imaging sensor and only moderate computing power.

In the multiple defect case of the third method, a special glass with randomised thickness must be placed before the sensor; its complexity defines pixel count in the sensor; visibility function randomisation of 33 % allows finding more than 60 % of defects at a sample distance of 1 mm in case of 199 pixel sensor. Doubling the pixel count can effectively reduce complexity of the glass, thus increasing the detection accuracy and allowing higher sensor distance to sample.

Computing hardware for the third method can effectively be implemented in FPGA due to parallel signal processing capabilities of this technology.

Further work will be continued to study result stability of CS approach versus noise of imaging matrix and ADC bit count. Practical research is needed to test real world applicability of the proposed methods in development of a defectoscope.

ACKNOWLEDGEMENTS

This research is financed by the European Regional Development Fund project (No.L-KC-11-0006) research 2.3. "Research in Thin Film Coating Technologies".

REFERENCES

1. Gonzalez, R. C., and Woods, R. E. (2008). *Digital Image Processing.* NJ: Pearson Prentice Hall.

2. McClellan, J. H., Schafer, R. W., and Yoder, M. A. (2003). *Signal Processing First*. NY: Pearson Prentice Hall.
3. Microscopy Resource Centre (2012). *Introduction to Deconvolution*. Available at http://www.olympusmicro.com/primer/digitalimaging/deconvolution/deconintro.html.
4. Donoho, D. L. (2006). Compressed sensing. *IEEE Transactions on Information Theory 52*(4), 1289–1306.
5. Candès, E.J., and Romberg, J. (2007). Sparsity and incoherence in compressive sampling. *Inverse Problems 23*, 969–985.
6. Gaigals, G., Greitans, M., and Andziulis, A. (2013). Compressive sensing: Analysis of signals in radio astronomy. *Baltic Astronomy*, *22*, 347–361.
7. Photometrics. (2010). *Keep the Noise Down*. Available at http://www.photometrics.com/resources/technotes/pdfs/snr.pdf.
8. Microscopy. *CCD Signal-to-Noise Ratio*. Available at http://www.microscopyu.com/tutorials/java/digitalimaging/signaltonoise/.
9. National Instrument. (2012). *Numeric Data Types Table.* Available at http://zone.ni.com/reference/en-XX/help/371361J-01/lvhowto/numeric_data_types_table/.
10. Russ, J. C. (2011). *The Image Processing Handbook*. UK: CRC Press.
11. Fornasier, M., and Rauhut, H. (2011). Compressive sensing. *Handbook of Mathematical Methods in Imaging* (pp. 187–228). NY: Springer.

MATEMĀTISKO MODEĻU IZSTRĀDE MIKRONA IZMĒRA TILPUMA DEFEKTU DETEKTĒŠANAI PLĀNO KĀRTIŅU PĀRKLĀJUMOS

G. Gaigals, M. Donerblics, G. Dreifogels

K o p s a v i l k u m s

Aprakstītais darbs ir saistīts ar matemātisku metožu izstrādi viena mikrona izmēra tilpuma defektu pozīciju noteikšanai stikla paraugiem, kas pārklāti ar plānajām kārtiņām, izmantojot attēlformēšanas paņēmienus, bet izvairoties no dārgām optiskām iekārtām, piemēram, lēcām.

Tika izstrādātas trīs metodes šādu defektu pozīciju noteikšanai, dots šo metožu apraksts. Metožu pārbaudei izveidoti simulāciju modeļi National Instruments grafiskās programmēšanas vidē LabVIEW.

Rakstā salīdzināti ar katru metodi iegūtie rezultāti, metožu precizitāte, ātrdarbība un implementācijas īpatnības. Iezīmēts turpmāko pētījumu virziens.

16.11.2015.

LATVIAN JOURNAL OF PHYSICS AND TECHNICAL SCIENCES
2016, N 2

DOI: 10.1515/lpts-2016-0013

APPLIED PHYSICS

DETERMINATION OF CONTACT POTENTIAL DIFFERENCE BY THE KELVIN PROBE (PART I)
I. BASIC PRINCIPLES OF MEASUREMENTS

O. Vilitis[1], M. Rutkis[1], J. Busenbergs[1], D. Merkulovs[2]

[1]Institute of Solid State Physics, University of Latvia, Riga, LATVIA
[2]Riga Technical University, Riga, LATVIA
e-mail: oskarsvil@gmail.com

Determination of electric potential difference using the Kelvin probe, i.e. vibrating capacitor technique, is one of the most sensitive measuring procedures in surface physics. Periodic modulation of distance between electrodes leads to changes in capacitance, thereby causing current to flow through the external circuit. The procedure of contactless, non-destructive determination of contact potential difference between an electrically conductive vibrating reference electrode and an electrically conductive sample is based on precise control measurement of Kelvin current flowing through a capacitor. The present research is devoted to creation of a new low-cost miniaturised measurement system to determine potential difference in real time and at high measurement resolution. Furthermore, using the electrode of a reference probe, the Kelvin method leads to both the indirect measurement of an electronic work function, or a contact potential of sample, and of a surface potential for insulator type samples.

In the article, the first part of the research, i.e., the basic principles and prerequisites for establishment of such a measurement system are considered.

***Keywords*:** *Kelvin probe, contact potential difference, surface potential.*

1. INTRODUCTION

At the end of 18th century, A. Volta conducted experiments on metal pairs and discovered the "contact electricity" that in modern language means the same as the contact potential difference (CPD) originating in the work function difference of two involved dissimilar electro-conducting materials. Volta revealed [1], if different metals are electrically connected in a sequential row and the temperature of all metals is equal, the potential difference between two external metals of this row does not depend on the other metal composition of this line. This potential difference is also known as the Volta potential. If the electrical contact is set between the outer end surfaces of metals in the row creating a closed loop, it follows from Volta law of serial contacts that the electric driving force in this circuit is equal to zero and the current

does not flow unless the temperature of all metals composing the circuit is equal.

It is possible to use the diagrams of electron energy levels (see Fig. 1) to explain the occurrence of contact potential difference.

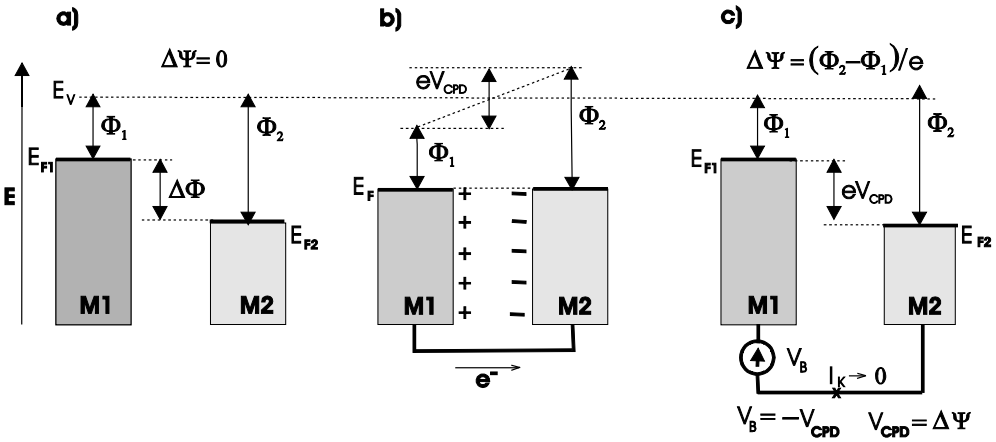

Fig. 1. Schematic representation of relationship between the contact potential difference (ΔΨ) and the work functions (Φ).

The metals (Fig. 1a) before being connected were electrically neutral, and two metals having different work functions Φ_1 and Φ_2 shared the same local vacuum level E_v. The work function Φ is defined as the minimum work needed to extract electrons from the Fermi level of a solid carrying a net charge [2], [3]. Upon the short-circuiting, the electrons of metals (Fig. 1b) are flowing to a metal with higher work function until the uniform redistribution of electrons at the Fermi levels E_{F1} and E_{F2} of both metals is reached. This leads to observation of Volta (or outer) potential difference ($\Delta\Psi$), which is equivalent to a difference of work functions of two metals, and in our case:

$$\Delta\Psi = (\Phi_1 - \Phi_2)/e, \tag{1}$$

where e is an elementary charge. Resulting voltage $V_{CPD} = \Delta\Psi$ compensates the work function difference by shifting the local vacuum level.

Figure 1(c) demonstrates that the shift of a local vacuum level can be compensated by an external "bucking voltage" (sometimes spelled "backing voltage"): $V_B = -V_{CPD}$. As the work function of metals is an intrinsic parameter, it remains constant after connection of two different metals [4], while the electrochemical potential of electrons within both phases becomes identical.

If the voltage V_B is chosen such that the electric field is eliminated (the flat vacuum condition), the Volta (or outer) potential $V_{CPD} = \Delta\Psi = (\Phi_1 - \Phi_2)/e$. Here, the potential V_{CPD} in volts (V) is equal to the energy $(\Phi_1 - \Phi_2)$ in electron-volts (eV) divided by an elementary charge (proton/electron charge) e.

Usually, the measuring device with the Kelvin probe uses metal (e.g. gold) as a probe, which is positioned within a short distance parallel to a flat sample material.

If the sample is a conductor, the contact potential difference $\Delta\Psi$ can be evaluated similarly (see Eq. (1)). The Kelvin method is based on the Fermi level equilibrium model.

If the electrode of Kelvin probe is a metal, the electron's exchange energy at the Fermi level inside a solid determines the bulk contribution of the main work function defined as the minimum work needed to extract electrons from the Fermi level of solid carrying no net charge [4]. It is accepted that the electron is removed at the end position (vacuum level) just outside the sample. In this case, it can be assumed that the electrons inside a bulk of any conductor can move freely, the free electrons are located on the surface of solid, the work function is mainly the surface property and CPD value is determined by (1).

However, the CPD between a sample end and a probe (reference electrode) is dependent not only on the material work function, but also on the surface conditions, such as contamition and deposition of a monolayer. The work is required for electron to pass the barier at the surface of a solid, which is made of the dipole layer in case of conductors and of the band bending in case of semiconductors. This should be considered studying materials at normal pressure in moist air, and polycrystalline materials and insulators.

In semiconductors, the position of the Fermi level is between the valence and conduction bands, and additional work is required to move the electron from the Fermi level to the conduction band. The work required for the electron to pass the barier at the surface of the solid, which is the dipole layer in case of conductors and the band bending in case of semiconductors.

If the sample is metal or semiconductor, the charge may be formed not only at the sample surface, but also at the boundary between the sample and the conductive or semi-conductive substrate electrode. Part of the charge can move through the sample volume, where sample polarisation and charge catching by the traps are possible.

If the insulators are involved, the measured value apart from chemical potential difference of reference metal and sample substrate metal depends also on insulator boundary surfaces and thickness-dependent potential fall on the insulator.

In these cases and the ones above, a more common description of the work function is its presentation like the sum of chemical work to transfer the electron from just outside the sample to the Fermi level (μ_e, chemical potential) and the electrostatic work to move an electron trough the dipol layer (χ, dipole or the surface potential), where e is an elementary charge [4]:

$$\Phi = -\mu_e + e\cdot\chi. \tag{2}$$

The Kelvin capacitor opposite materials (sample and gold-reference) are connected to each other through the outer circuit, so that the electrochemical potentials of electrons are in equilibrium. Therefore, the external potential difference at bucking voltage $V_B = 0$ (Fig. 1b) is [5]:

$$e(\Psi_1-\Psi_2)= (\mu_{e1}- e\chi_1) - (\mu_{e2}- e\chi_2) = \Phi_2-\Phi_1. \tag{3}$$

In respect to the measured values of Kelvin method, it is important to distinguish them when the difference of contact potentials or the difference of surface potentials is involved, and when the difference of work functions is concerned [5]. These conceptualisations initially apply to homogeneous surfaces.

As it has already been noted, if one electrode of the Kelvin condenser is connected to another, the electron diffussion begins from the electrode material with a higher Fermi level to the material with a lower one. At a time of level equalisation, the electrical potential on the electrode with a lower Fermi level is growing, and it is decreasing in the opposite case, thereby contact potential difference of the Kelvin condenser between electrodes is increasing. Without this outer Volta potential, the potential leap, i.e. the electrical field, arises directly at the place where both condenser electrodes are connected, which resists to the process of electron diffusion. If this inner contact potential difference reaches a certain value, the electron diffussion stops and Fermi levels of both electrode materials equalise. To let the electrical charge e pass the phase boundary from the material "just inside the bulk" to one "outside the sample", it is necessary to do the work $e\chi$.

Thereby, the material electronic work function Φ is given by a sum of the chemical potential just inside the bulk μ_e and the electrical potential outside the sample χ, as it has been mentioned (2). The surface potential is forming on the sample surface, but at the distance l outside the surface it is gradually decreasing to zero, which is determined by the amount of free electrons compensating the charge carriers. The distance l depends on the electrode material and on the presence of other surfaces and boundary phases, which could be located close enough to cause the mutual influence. Ignoring this fact, it can lead to errors when interpreting measurement results. The surface charge of metals is compensated by the free electrons outside the material surface at a distance of some atomic diameters, forming a few Å thick dipole layer.

For semiconductors, the part of required charge for compensation is located at an extended boundary layer of the space charge zone. In this case, the Debye length $l = \delta_D$ can expand up to 1 μm [5]. Therefore, it is possible to split the work function in a purely chemical work μ_e and a purely electric work $e\chi$.

On the other hand, it can also be divided: into the difference of conduction and valence bands $E_C - E_F$, the band bending eVs and the electron affinity ξ [5]:

$$\Phi = (E_C - E_F) - eV_S - \xi \, . \tag{4}$$

If for semiconductors it is possible to interpret the measured value of two material contact potential differences as a difference of material two work functions, this interpretation is not applicable to insulators. For insulator samples without chemical potential difference of probe material and insulator grounding metal $\Delta\mu$, the measured potential difference $\Psi_{ISOL} - \Psi_{REF}$ also comprises the potentials on the insulator boundary surfaces χ_1, χ_2 and thickness-dependent potential curve V_S on the insulator [5].

$$\begin{aligned} &e(\Psi_{ISOL} - \Psi_{REF}) = (\mu_{eM} - e\chi_1 - e\chi_2 - V_S) - (\mu_{eREF} - e\chi_{REF}) = \\ &= \Delta\mu - e\,(\chi_1 + \chi_2 + \chi_{REF}) - eV_S. \end{aligned} \tag{5}$$

It is worthwhile to examine the validity of relation (1) for metal-semiconductor Kelvin probe arrangement in detail. In the isolated semiconductor, the surface band bending is determined by the free surface charge neutrality condition $Q_{ss} + Q_{sc} = 0$, *where* Q_{ss} *is the net surface charge and* Q_{sc} *is the net charge in the surface charge region (both per unit area).* If the metal is connected to the back side of a semiconductor, the MIS structure (metal-isolator-semiconductor) is formed.

For example, in this case, it is possible to analyse whether the semiconductor band bending and, thus, its work function are changed. The appropriate charge neutrality condition becomes $Q_m + Q_{ss} + Q_{sc} = 0$, where the effect of Q_m (*charge density on the metal + insulator surface)* may be significant if the width of the capacitor gap is not much larger than the width of the surface depletion region [6]. Therefore, the potential energy drop across the capacitor gap may be modified to $eV'_{CPD} = (\Phi'_1 - \Phi_2)$ (where Φ'_1 is the modified work function of a semiconductor) instead of $eV_{CPD} = (\Phi_1 - \Phi_2)$. However, the magnitude of external DC bias voltage V_B required to discharge the capacitor remains equal and opposite to the real contact potential difference V_{CPD} rather than to V'_{CPD}. It happens because if the capacitor is discharged, Q_m by definition is zero, the charge neutrality condition reduces to that of a free surface, and the semiconductor work function returns to its original value.

Nearly a hundred years passed since Volta had demonstrated the contact "electricity", while Lord Kelvin, 1898 [7], discovered possibility to measure the CPD also quantitatively. He used the condenser with plates of two various metals, as well as an electrometer, and it was for the first time when the direct measuring of CPD had been carried out compensating the measured potential difference with a variable outer voltage source (null-method). Zisman first applied this principle in the form of the vibrating capacitor in 1932 [8], which, in comparison with manual compensation arrangement, speeded up CPD measuring several times. And only then this method became widely applied in practice. In this case, the contact potential difference between the Kelvin probe and the conductive sample is equal to the applied compensation voltage.

Determination of the surface electric potential difference by the Kelvin probe, i.e. vibrating capacitor technique, is one of the most sensitive measuring procedures in surface physics. For instance, the Kelvin probe force microscopes and the scanning tunneling microscopes were modified to obtain a high-resolution data of electric surface potential distribution.

Due to its extremely high surface sensitivity, this method is used in many different areas of modern chemistry and physics to measure and analyse the surface characteristics of conductors, semiconductors, insulators, chemicals, biochemicals, photochemicals, chemical sensors, biosensors, biochemical microarrays, electronic image devices, micromachined devices, nanodevices, corroded materials, coatings, adsorbed materials, contaminated materials, oxides, thin films, liquid interfaces, self-assembling monolayers, and others [9]. The method is also applied to investigate semiconductor doping [10] and to study energy-level alignment of conjugated polymers deposited on various electrodes [11]. Besides, the further systems application was provided to measure and analyse different organic molecules and thin films [12]. The method is also used for high-resistivity non-polar and polar molecules deposited on both gold and ITO glass electrodes. The voltage drop over the capacitor formed by an organic layer and reference electrode is given [13].

2. BASIC PRINCIPLES UNDERLYING THE MEASURING SYSTEM

The Kelvin method is one of the most commonly used for CPD measuring. This contactless non-intrusive method is based on using the traditional Kelvin probe (see Fig. 2a) placed in plane-parallel to the stationary sample electrode at a distance d_0 shaping the simple two-plate capacitor.

To measure CPD, in accordance with the law of Volta's serial contacts, it is necessary to connect a variable voltage source V_B and a series resistor R_{IN} via an external circuit (see Fig. 2a). Due to difference in work functions of different electrode materials, CPD must be measured in an open circuit, i.e., using the dielectric such as vacuum or air between the surfaces of inner plates $V_{CPD}=\Delta\Psi$. To improve the resolution of a sample surface scanning, a small probe surface is required. The orientation of Kelvin probe surface area with respect to a sample surface is analogous to a parallel plate capacitor, whose capacitance C is defined:

$$C = (\varepsilon_o \cdot \varepsilon_r \cdot A) / d_0, \tag{6}$$

where ε_0 is a dielectric constant, A is an area of Kelvin probe and d_0 is a distance between plates. The dielectric constant ε_r for measurements in air or vacuum is assumed to be 1.

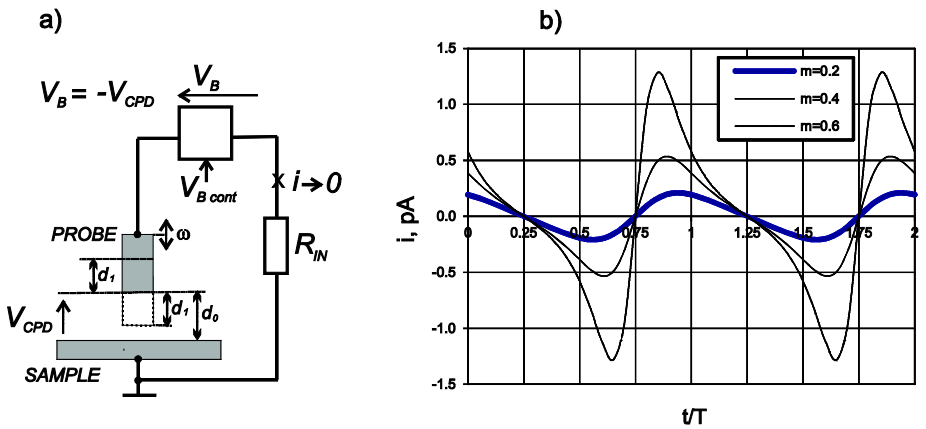

Fig. 2. Schematic of the Kelvin probe input stage: a) variable applied bucking potential V_B source block with its control voltage V_{Bcon}, i – the current in Kelvin probe outer circuit R_{IN}, V_{CPB} – the contact potential difference between Kelvin condenser inner electrodes PROBE and SAMPLE, d_0 – the mean distance between the sample and the probe, d_1 – the amplitude of the probe vibration depending on time t expressed in vibration periods. b) The wave form of current $i(t)$, see Eq. (11) for different values of modulation factor m. It illustrates the appearance of Kelvin probe signal oscillograms.

If the voltage V_{CPD} caused by Kelvin condenser inner surface potentials is constant, the condenser charges at charge Q:

$$Q = C \cdot V_{CPD}. \tag{7}$$

The Kelvin probe is stimulated to a sinusoidal vibration around the average distance d_0 between Kelvin probe electrode and the sample surface with amplitude d_1 ($d_1 < d_0$) and frequency ω expressed in radians.

Kelvin probe location changes with time, hence:

$$d(t) = d_0 + d_1 \cdot \sin(\omega t). \tag{8}$$

Ratio d_1 to d_0 characterises the amplitude of current signal and is referred to the modulation factor m:

$$m = d_1 / d_0. \tag{9}$$

It follows from Eqs. (6), (7) that the charge Q will change along with changes of Kelvin probe capacity resulting in change of current $i(t)$ in the outer circuit, which at the bucking voltage $V_B = 0$ and $V_{CPD} \neq 0$ reproduces current:

$$i(t) = dQ/dt = V_{CPD} \cdot dC/dt. \tag{10}$$

Substituting Eqs. (6)–(8) into Eq. (7), the current signal i(t) can be expressed as:

$$i(t) = V_{CPD} \cdot \varepsilon_0 \cdot \varepsilon_r \cdot A \cdot [m \cdot \omega \cdot \cos(\omega t)] / [1 + m \cdot \sin(\omega t)^2]. \tag{11}$$

In the conventional nulling technique [14], the variable bucking potential V_B is adjusted until the Kelvin current vanishes $i \rightarrow 0$. V_B is equal and opposite to V_{CPD}, the electric field between the Kelvin capacitor electrodes is compensated and the zero output signal is recorded, wherein the ac current in the Kelvin probe outer circuit drops to zero: $i(t) = (V_{CPD} + V_B) \cdot dC/dt = 0$ if $V_{CPD} = -V_B$.

Determination of voltage V_{CPD} caused by a contact potential difference on the vibrating electrode of capacitor in the systems with the Kelvin probe is asociated with involving of the compensating voltage V_B in the capacitor external circuit, at which the Kelvin current $i(t)$ disappears. In this case, the absolute value of signal V_{CPD} comes into balance with a value of voltage V_B and V_{CPD} polarity is opposite to polarity V_B. However, the exact measurement of the equilibrium point V_{CPD} is getting more complex by the fact that at this area the signal-to-noise ratio reaches minimum by $i(t) \rightarrow 0$, and the noise creates the biasing voltage, thereby causing measurement errors. Therefore, the present conventional V_{CPD} measuring systems use the "off-null" algorithm, where the Kelvin probe signal is measured at two or more values of V_B, for instance, at high signal levels, and the balance point is obtained by extrapolation.

However, this accurate nulling technique also has several disadvantages, as we have already pointed out above. Thus, the statistical linear correlation-regression analysis, despite its high complexity in case of an area scan with a few hundred measurement points, first of all requires completing a set of all measurements. Thus, the online monitoring of the contact potential difference is not possible and the result of the measurement can be analysed only after the experiment is finished. Furthermore, the above-mentioned modified off-null technique implementation is generally associated with a need of a PC with pre-installed extensive software and use of the

external data acquisition digital control unit with a host PC data acquisition system housed in the PC system, which not only increases the extent and the weight of the measuring equipment but also raises production costs and, therefore, limits the wider use of the Kelvin probe.

We have indicated a new and simple way that allows determining the contact potential difference by entering the composite and time-varying bucking voltage in the Kelvin probe measuring circuit.

The results of experimental measurement system test for determination of the contact surface potential difference in the range of + 10,000 V up to –10.000 V have shown the stable measurement resolution in the range of ± (1–2 mV) (See Part 2 of this article in one of the upcoming journals).

3. CONCLUSIONS

The basic characteristics and principles for determination of contact potential difference using the Kelvin probe and the preconditions for development of such a measurement system have been considered, namely:

- under the following conditions, the measured value is the difference between outer potentials of two materials of Kelvin capacitor electrodes. If these materials are metals or semiconductors, the measured value can be interpreted as a difference between the work functions of these materials. The charge can be formed not only at the sample surface, but also at the boundary between the sample and the conductive or semi-conductive substrate electrode. Part of the charge can move through the sample volume, where sample polarization and charge catching by the traps is possible. If the insulators or semiconductors with low electrical conductivity are involved, the measured value apart from chemical potential difference of reference metal and sample substrate metal also depends on insulator boundary surfaces and thickness-dependent potential fall on the insulator.
- the main principles and conditions, underlying the measuring systems and assessment of their effectiveness.

REFERENCES

1. Volta, A. (1800). On the electricity exited by the mere contact of conducting substances of different kinds. *Philos. Mag. 7***,** 298–311.
2. Maljusch, A., Henry, J.B., Tymoczko, J., Bondarenka, A.S., and Schuhmann, W. (2013). Towards linking basic surface properties with electrocatalytic activity. *Electronic Supplementary Material (ES) for RSC Advances,* 1–3.
3. McNaught, A.D., and Wilkinson, A. (1997). IUPAC. *Compendiom of Chemical Terminology*. Oxford: Blackwell Scientific Publications.
4. Maljusch, A. (2012). Integrated scanning Kelvin probe – scanning electrochemical microscopy system: design, development and applications. *Diss*., 1–245.
5. Ostrick, B. (2000). Die Untersuchung der Karbonat – Kohlendioxid – Wechselwirkung im Feuchtefilm der Oberfläche. Diss., 1–131.

6. Kronik, L., and Shapira, Y. (1999). Surface photovoltage phenomena: theory, experiment, and applications *Surf. Sci.e Rep. 37***,** 1–206.
7. Thomson, W. (later Lord Kelvin) (1898). Contact electricity of metals. *Philos. Mag.* 46, 82–120.
8. Zisman, W.A. (1932). *Rev Sci. Instrum.* ***3***. 367–370.
9. Thompson, M., and Cheran, L.E. (2006). Scanning Kelvin microprobe system and process for analyzing a surface. *US Patent Nr. US 7084661 B2.*
10. Filipavičivs, V., Gaidys, R., Matulaitis, V.A., Petrauskas, G., Sakalas, A., and Sakalauskas, A. (1987). Investigation of the surface states in heavily doped GaAs by Kelvin probe. *Phys. Stat. Sol. 99*, 543–547.
11. Lange, I., Blakeslay, J.C., Frisch, J., Vollmer, A., Koch, N., and Neher, D. (2011). Band bending in conjugated polymer layers. *Phys. Rev. Letters* 106, 216402-1–216402-4.
12. Vilitis, O., Fonavs, E., and Muzikante, I. (2001). A system for measuring surface potential by the Kelvin-Zisman vibrating capacitor probe. *Latv. J. Phys. Techn. Sci.* ***5***, 38–56.
13. Pfeiffer, M., and Leo, K. (1996). Fermi level determination in organoc thin films by the Kelvin probe method. *J. Appl Phys. 80* (12), 6880–6883.
14. Ritty, B., Wahtel, Ott, F., Manquenouille, R., and Donnet, J.B. (1980). New application of the Kelvin method involving the scanning of the bucking voltage. *Rev. Sci. Instrum.* ***51*** (10), 1421–1423.

KONTAKTPOTENCIĀLU STARPĪBAS NOTEIKŠANA AR KELVINA ZONDI (I DAĻA)
1. MĒRĪŠANAS PAMATPRINCIPI

O. Vilītis, M. Rutkis, J. Busenbergs, D. Merkulovs

Kopsavilkums

Kontaktpotenciālu starpības izraisītā sprieguma V_{CPD} noteikšana uz vibrējoša kondensatora elektrodiem sistēmās ar Kelvina zondi ir saistīta ar tāda kompensējoša sprieguma V_B iesaistīšanu kondensatora ārējā ķēdē, pie kura izzūd Kelvina strāva $i(t)$. Šajā gadījumā signāla V_{CPD} absolūtais lielums nonāk līdzsvarā ar sprieguma V_B lielumu un tā polaritāte ir pretēja V_B polaritātei. Taču precīzu V_{CPD} mērīšanu līdzsvara punktā sarežģī tas, ka, ja $i(t) \rightarrow 0$, signāla un trokšņa attiecība sasniedz minimumu, un trokšņi rada nobīdes spriegumu un līdz ar to kļūdas mērījumā.

Tādēļ patlaban konvencionālajās V_{CPD} mērīšanas sistēmās izmanto t.s. ´off-null´ algoritmu, pie kura Kelvina zondes signālu vispirms mēra, piemēram, pie divām vai vairākām augstākām signāla V_B vērtībām un pēc tam atrod minēto līdzsvara punktu ekstrapolācijas ceļā.

Taču arī šādam precīzam nullēšanas paņēmienam piemīt daži trūkumi. Tā, ja skenējamā parauga apgabalā tiek ietverti vairāki simti mērīšanas punkti, statistiskā korelācijas un regresijas analīze, neraugoties uz tās augsto sarežģītības pakāpi, prasa, lai vispirms būtu veikts pilns visu mērījumu kopums. Tādējādi, nav iespējama

operatīva kontaktpotenciālu starpības monitorēšana, jo mērījumu rezultātus var analizēt tikai pēc eksperimenta pabeigšanas. Bez tam, iepriekšminētā modificētā ′off-null′ paņēmiena realizācija parasti ir saistīta ar nepieciešamību izmantot datoru ar tajā iepriekš instalētu plašu programmatūras nodrošinājumu un ārējo datu ieguves digitālo vadības bloku ar hostdatorā izvietoto datu ieguves sistēmu. Tas ne vien palielina mērīšanas aprīkojuma apjomu un svaru, bet arī paaugstina ražošanas izmaksu un, līdz ar to, ierobežo Kelvina zondes plašāku pielietojumu.

Esam norādījuši jaunu un vienkāršu veidu, kas ļauj nepārtraukti noteikt kontakta potenciālu diferenci V_{CPD}, regulāri ievadot Kelvina zondes mērīšanas ķēdē kompozītu un laikā mainīgu pretspriegumu V_B (skatīt šī raksta otro daļu kādā no turpmākajiem žurnāliem). Eksperimentālie mērīšanas sistēmas testa rezultāti pa noteiktu kontakta virsmu potenciālu starpības robežās no + 10,000V līdz -10.000V ir parādījuši stabilu ± (1–2 mV) mērījumu izšķirtspēju.

18.01.2016.

LATVIAN JOURNAL OF PHYSICS AND TECHNICAL SCIENCES
2016, N 2

DOI: 10.1515/lpts-2016-0014

HARDWARE DESIGN OF THE ENERGY EFFICIENT FALL DETECTION DEVICE

A. Skorodumovs, E, Avots, J, Hofmanis, G. Korāts

Ventspils University College,
101 Inzenieru Str., Ventspils, LV-3601, LATVIA

Health issues for elderly people may lead to different injuries obtained during simple activities of daily living. Potentially the most dangerous are unintentional falls that may be critical or even lethal to some patients due to the heavy injury risk. In the project "Wireless Sensor Systems in Telecare Application for Elderly People", we have developed a robust fall detection algorithm for a wearable wireless sensor. To optimise the algorithm for hardware performance and test it in field, we have designed an accelerometer based wireless fall detector. Our main considerations were: a) functionality – so that the algorithm can be applied to the chosen hardware, and b) power efficiency – so that it can run for a very long time. We have picked and tested the parts, built a prototype, optimised the firmware for lowest consumption, tested the performance and measured the consumption parameters. In this paper, we discuss our design choices and present the results of our work.

Keywords: *3-axis accelerometer, electronics, energy efficiency, fall detection, hardware, microcontroller, telecare.*

1. INTRODUCTION

A fall is a dangerous event and may produce a variety of ill effects (such as concussion, fractures, ruptures, internal hemorrhaging), especially for the elderly people. According to [1], [2], it is estimated that over a third of adults older than 65 years fall each year, making it the leading cause of the injury or even death for that age group. As falls generally are uncontrolled and sometimes are caused by specific diseases, the injured person may remain unconscious, incapacitated or otherwise unable to request assistance. Several studies [3], [4] have concluded that elderly people, who choose to live at home, are also willing to accept new technologies to support their sovereignty and safety.

Fall detection methods usually are divided into three categories [5]: wearable sensors, ambience sensors and vision (camera) based sensors. Only wearable systems provide all necessary conditions for live telecare monitoring, where the main concern is the cost of the sensor device and system's setup.

Fall detection device is an accelerometer and/or gyroscope based wearable

unit, used in telecare for patient activity monitoring and fall detection. The main function of the fall-detection device is to recognise the abnormal acceleration or orientation, run the fall recognition algorithm on the recently acquired data set, and if the fall is detected – send a distress signal to the monitoring station. Most of the fall detection devices also have a "panic button", which allows the patient to request assistance in other situations.

The device consists of hardware and firmware parts. In this paper, we focus on the hardware design and implementation, so the firmware will only be briefly discussed when device functionality and power consumption are concerned.

2. RESULTS AND DISCUSSION

2.1. System Overview

The core components of our fall detection device are: LIS2DH – low power consumption accelerometer [6]; ATxmega32C4 – a 16-bit Flash-based microcontroller with a selection of sleep modes and consumption reduction settings [7], capable of running the fall detection algorithm; nRF24L01+ [8] module – a short range 2.4GHz RF communication module; and MAX1724 – DC/DC step-up converter with low quiescent current and high efficiency at light load [9].

It should be mentioned that we chose ATxmega32C4 both for its characteristics (1-2uA consumption in sleep mode, acceptable voltage range, pin count, TQFP and smaller VQFN package availability, acceptable price – 2.45 € w/o VAT, built-in USB module for debug data output, and 32KB program memory) and our experience in working with Atmel devices and their integrated development environment (IDE). The LIS2DH was chosen because of its low power consumption in low frequency modes, small LGA-12 footprint and wide range of sensitivity, resolution and frequency settings, which came in handy in the fall detection algorithm development phase. The RF module was chosen mainly because it was a compact low-budget solution and allowed for 2Mbps debug data transmission, while having relatively low power consumption. The 2.4GHz frequency is suitable for patch and chip antennas, making the module small enough (18x12mm) for our prototype. The device schematic may be observed in Fig. 1.

2.2. Fall Detection Algorithm

Figure 2 shows the device behaviour in the active mode when triggered by a free-fall event. Before the interrupt, the accelerometer (ACC) gathers high-resolution (12b) data in internal "first in, first out" buffer (FIFO) at 25Hz frequency, while constantly checking for a free-fall condition using a simple built-in state machine. When the ACC recognises the free-fall event, it generates an interrupt to wake up the microcontroller unit (MCU). The MCU then becomes active, acquires last 32 samples from the ACC to calculate the orientation, configures the ACC to a higher

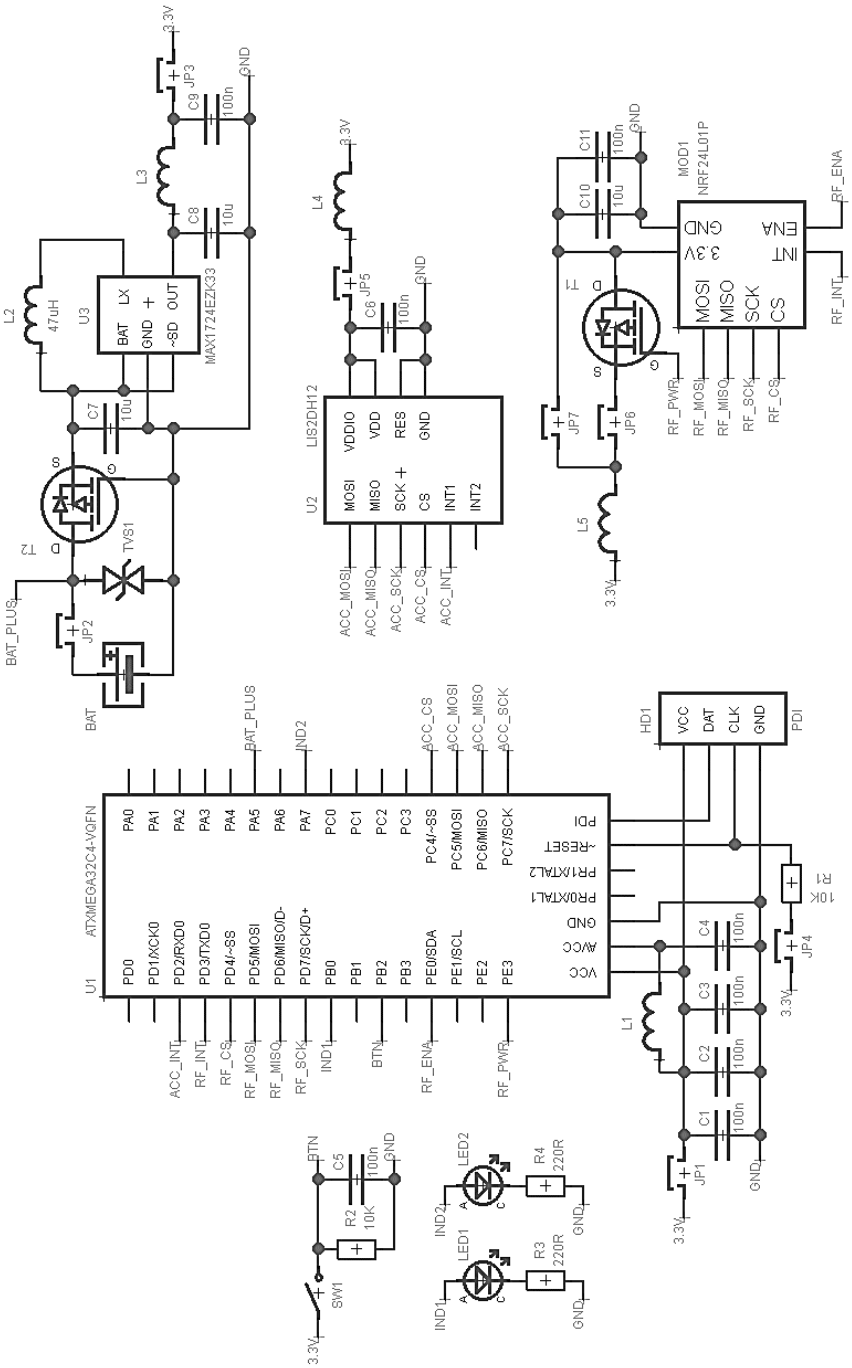

Fig. 1. Device schematic.

frequency (100Hz) and returns to power-save mode for 320ms to conserve the energy. When ACC 32 level FIFO is full, the MCU wakes up to acquire the samples and calculate Teager energy operator (TEO). This cycle is normally repeated four times in order to obtain >1 s (1.28 s) data set. After that, if TEO exceeds the threshold and impact is detected, orientation check is performed. If device orientation has changed

by more than 60 degrees, the event is regarded as the "true-positive" – MCU powers up the RF module, sends the distress signal and waits for acknowledgement from a base station. When acknowledgement is received, the MCU returns to sleep. If the acknowledgement is not received, the device will keep sending messages trying to contact the station. If TEO has not tipped the threshold or the orientation has not changed, the event is considered a "false-positive" response, and MCU goes back to sleep [10].

Notice that the algorithm is designed in such a way that a continuous free-fall condition will reset the data acquisition and TEO calculation cycle. This may result in longer active cycles in some cases, which will be discussed later.

Another point to mention is the so-called "panic button", which is simply a tact switch located in the front panel, which wakes up the MCU to send a manually triggered distress signal to the base station.

The two light-emitting diodes (LED) on the front panel are used for indication. The green LED lights up when the device is trying to contact the base station. It is necessary in order for user to know that the device is operational and trying to make contact with the station. The amber LED lights up when the acknowledgement from the base station was received, so that a user would know that his distress signal was heard and the help was on its way.

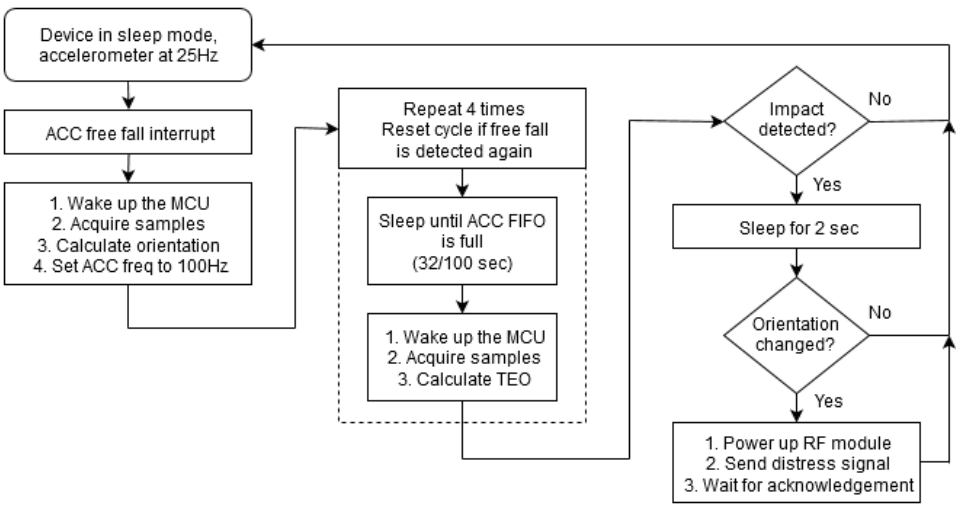

Fig. 2. Fall detection algorithm.

2.3. The Power Source

There is a number of trade-offs one must consider when designing a power circuit for a wearable device: rechargeable or non-rechargeable battery, 3.0-3.6V or 1.4–1.6 V, single or dual cell solution, cell chemistry, size, weight, energy density, availability and price range must be considered.

We have decided to use alkaline instead of lithium-based cells. Though lithium cells have high energy density and the output voltage is just right for 1.7– 3.6 V

digital circuitry, we have had major safety concerns about them. Since the device is wearable, it might prove inconvenient if the cell caught fire or exploded due to overheat when accidentally pressed against a hot surface, or due to internal discharge caused by protection circuit malfunction or damage caused by electrostatic discharge (ESD).

The second decision was to use non-rechargeable batteries. One of the main reasons is that at the moment (Sept. 2015) non-rechargeable alkaline batteries provided twice the power of rechargeable Nickel Metal Hydride (NiMH) batteries for one fourth of the price. VARTA non-rechargeable alkaline 1.5 V AA cell provides 2.85 Ah at the cost of approximately 1.60 € (including VAT), while VARTA rechargeable NiMH 1.2 V AA cell provides only 1.6 Ah at the cost of approximately 6.70 € (including VAT). Non-rechargeable alkaline batteries are readily available and may be discharged down to 0.8 V (limited by a DC/DC converter), while NiMH have a high self-discharge rate and may only be discharged down to about 1.0 V to prevent battery damage. Rechargeable battery based solution would also require over-discharge protection, an external battery charger, or additional recharging circuitry and a DC power source. Our preliminary average current consumption estimation was average 100 uA at 3.3 V, with 65 % upconverter efficiency, so life expectancy (not including high NiMH cell self-discharge rate and alkaline cell deep discharge option) of the alkaline battery might roughly be about 350 days, while NiMH should last almost 160 days. This rough estimation was necessary to assess the need for device maintenance and viability of both solutions. The actual battery discharge is monitored by MCU and reported regularly during operation. We have decided that using non-rechargeables would simplify the circuitry and therefore allow for easier routing, minimise printed circuit board (PCB) size, reduce component costs, and reduce device maintenance frequency and expenses associated with it.

Using multiple cells for higher voltage does not seem to be a viable option, since even a single 24 g AA cell (by the authors' personal account) is almost too heavy for a wearable sensor. It is for these reasons that we have decided to focus our design on a single alkaline AA or AAA cell as a power source. One thing worth mentioning is that because of said integrated circuit (IC) supply voltage range (1.7–3.6 V), it is impossible to power the device with a single alkaline cell (1.5–1.6 V when full). Powering from 3.0–3.6 V lithium cell is possible if precaution measures are in place to limit the voltages exceeding the IC's maximum. This approach may be cheaper, but may not be an effective solution. Battery output remains above or at the rated voltage for the most of the operational time, and digital circuitry consumption almost does not depend on supply voltage, so converting the 3.6 V battery output to 3.0 V with 87–90 % efficiency would still provide a power boost. The viability of this approach highly depends on battery and LDO choice and requires additional research and testing to give a definitive answer, but is out of the scope of this topic, since we have already settled on a single alkaline cell.

When a device has no external power source and only relies on a battery, the current consumption becomes one of the primary issues. Many modern ICs have a range of power reduction settings and modes, which disable unused features and parts of internal circuitry, thus reducing power consumption. Further in the text we differentiate between "sleep" and "active" modes. Active mode is when all calcula-

tions, interfacing and data exchange take place. In the sleep mode, the accelerometer collects data and checks for the free-fall condition at the minimal frequency allowed by the algorithm, while the MCU is in the power-save mode.

2.4. DC/DC Converter

The next step in designing the device was to choose the suitable DC/DC converter for the application. We have estimated that in the sleep mode our design should consume no more than 50 uA, while in the active mode, the average consumption might be about 10 mA, lasting 0.5 s per each false-positive wake-up. The false-positive wake-up is an event, when MCU becomes active, acquires and analyses accelerometer data, but the algorithm concludes that no actual fall has happened, and, therefore, no distress message will be sent.

We have done a test run that resulted in up to 60 false-positive wake-ups per hour for a very active and lively person (driving a car, jumping, walking, sitting down and getting up, riding elevator up and down, walking up and down the stairs, etc.). A simple calculation shows that if the person sleeps 8 h per day and maintains this high level of activity during all other hours (which is not very likely), the active mode current consumption (at DC/DC converter output) would be 4800 mAs, while the sleep mode would consume 4320 mAs. For an actual ill or elderly person, the passive consumption would therefore always dominate over active, so the primary concern for DC/DC converter should be conversion efficiency at light loads.

Based on availability, cost and datasheet parameters, such as high efficiency, low quiescent current, and input voltage range, we have selected four potential step-up converters from well-recognised manufacturers: MAX1724EZK33+T, NCP1400ASN27T1G, TPS61221DCKT, and LTC3525ESC6-3.3. We have tested them for conversion efficiency at 300 R, 3 K, 30 K, 300 K loads, with 10 uH, 15 uH, 22 uH, 47 uH inductors, at 0.7 V, 1.0 V, 1.6 V input voltages. It should be mentioned that with NCP1400A and LTC3525, only inductors fitting in manufacturer specified range were tested. Another thing to mention – NCP1400A output voltage is 2.7 V, while others supply 3.3 V. In most tested cases, higher external inductance increases converter efficiency. The device in the sleep mode was represented by 300 K–30 K load range, and 300 R – in the active mode. Characteristics of MAX1722 with 47 uH (66–85 % efficiency in sleep, 87–96 % when active) were best suited for the design of the device in question.

2.5. Energy Consumption Reduction and Measurements

The central part of the design is the accelerometer. Upon MCU wake-up, the algorithm requires 1 second long data backlog with the highest possible time resolution, which can only be achieved by configuring the device in 25Hz mode with output to internal 32-level FIFO. Datasheet states that in high-resolution 25 Hz mode LIS2DH should consume only about 6 uA, which is consistent with our prototype measurements [6].

Another crucial part of the design is the microcontroller. Datasheet states that in power-down and power-save modes (at 25 °C) ATxmega32C4 MCU with 3 V power source should consume less than 1 uA, if using external clock and all power saving options are enabled [7]. The device should report battery condition to the base station at least few times a day, so it is impossible to use the least consuming "power-down" mode. In this mode, only asynchronous interrupts can wake up the controller. All internal circuitry, including clock sources, timers and counters, necessary to wake up the MCU to measure and report the battery status, is disabled. Power-save mode consumes more power, but allows keeping operational the circuitry necessary for a timed wake-up. Our measured results for power-down: 0.44 uA, power-save: 1.37 uA, standby: 77 uA, idle: 282 uA, active 848 uA.

3. TEST DATA AND BATTERY LIFE EXPECTANCY

Table 1 shows sleep and active mode current consumption measured in the device prototype. Battery consumption was measured at 1.56 V.

Table 1

Measured Device Power Consumption (% – Mode Efficiency)

Parameter	Consumption	Parameter	Consumption
Accelerometer sleep current	5.9 uA	False-positive consumption	3714 ms at average battery drain 386 uA (2236 uWs, 87 %)
Microcontroller sleep current	1.4 uA	Additional data read consumption	320 ms at average battery drain 925 uA (462 uWs, 82 %)
RF module sleep current	0.1 uA	RF message sent	44 ms at average battery drain 4.52 mA (310 uWs, 90 %)
Reset pin pull-up current	0.1 uA	RF message received	12.8 ms at average battery drain 4.28 mA (85 uWs, 92 %)
Converter output current at sleep	7.5 uA at 3.3 V (24.75 uW)	Single LED current	4-5 mA, 9.6–12.2 mA (15–19 mW) battery drain per second
Battery output current at sleep	24 uA at 1.56 V (37.44 uW, 66 %)	"Panic button" current	0.33 mA, 0.84 mA (1.3 mW) battery drain per second

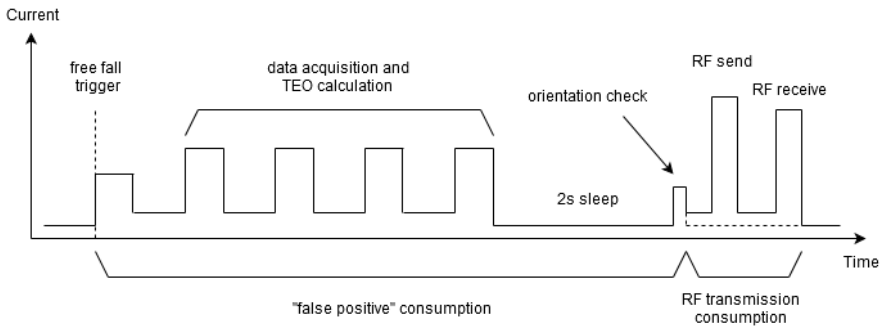

Fig.3. Device active mode current consumption explanation.

Figure 3 shows the current consumption when the device is in the active mode. The false-positive consumption with a single free-fall trigger drains 2236 uWs during approximately 3720 ms. The true-positive cases with RF transmission will happen relatively rarely and can be neglected. It has previously been mentioned that in data acquisition and TEO calculation phase the algorithm can be restarted and active consumption may therefore increase. Our tests show that during everyday activities this usually happens when walking down the stairs or taking an elevator. For example, we have detected up to 41 additional consecutive free-fall events while riding the elevator down for about 13–15 seconds. Since elevator constantly moves, the cycle restarts after the first data read cycle. This results in 21.2 mWs battery drain. Fast walk down the stairs results in 1 to 7 consecutive triggers per stair (5 on average, depends on the walking rate). Due to nature of a person's movement, we are assuming that an average of 2.5 ACC data read cycles pass before restarting the algorithm, resulting in 6.9 mWs battery consumption. Other actions normally produce only a single free-fall trigger and only consume 2.2 mWs. The sleep mode consumption is 37.44 uW, resulting in 0.9 mWh daily battery drain.

A very lively person could drain the battery for up to 0.78 mWh+0.9 mWh=1.68 mWh per day. A less active elderly person would drain the battery for 0.07 mWh+0.9 mWh=0.97 mWh daily. Comparison of active and passive power consumption proves our previously made assumption that light load (sleep mode) performance is paramount for this design.

The previously mentioned VARTA Industrial alkaline battery is rated for 3.3 Wh worth of energy at 43 Ohm load with 0.9 V end voltage [11]. Compensating 25 % for DC/DC converter's decreased efficiency at lower input voltages and battery self-discharge, this should result in 4 to 7 years of operation, depending on person's activity and not including true-fall event consumption and daily battery condition reports. The number is impressive, but it should be noted that only after extensive device testing in real operating conditions and obtaining the normal and abnormal event statistics, it will be possible to calculate more realistic battery life expectancy.

4. CONCLUSION

The main goal of the present research – the design of an energy efficient fall detection device – was successfully completed. The prototype was built and tested for functionality. There is space for improvement though:

1. The main power consumer in the sleep mode is the accelerometer. It is drawing almost 6 uA of current. Other accelerometers with comparable functionality and resolution may be considered for replacement.
2. A way to reduce the power consumption is to pick a converter with lower output voltage and comparable (50–70 %) output efficiency. If a better converter for 1.71 V output is used, the battery life may be extended significantly.
3. A buzzer might prove useful to provide additional audio feedback from a device to a user.

ACKNOWLEDGEMENTS

The present research has been financed by European Regional Development Fund project's (No.L-KC-11-0006) research 2.8. "Wireless Sensor Systems in Tele-Care Application for Elderly People". The authors also thank the Municipality of Ventspils City for additional support.

REFERENCES

4. Hornbrook, M. C., Stevens, V. J., Wingfield, D. J., Hollis, J. F., Greenlick, M. R., and M. G. Ory. (1994). Preventing falls among community-dwelling older persons: results from a randomized trial. *The Gerontologist 34* (1), 16–23.
5. Heinze, C., Halfens, R. J. G. and Dassen, T. (2007). Falls in German in-patients and residents over 65 years of age. *Journal of Clinical Nursing **16.3***, 495–501.
6. Brownsell, S.J., Bradley, D.A., Bragg, R., Catlin, P., and Carlier, J. (2000). Do community alarm users want telecare? *Journal of Telemedicine and Telecare **6***, 199–204.
7. Brownsell, S., and Hawley, M.S. (2004). Automatic fall detectors and the fear of falling. *Journal of Telemedicine and Telecare 10*, 262–6.
8. Muhammad, M., Shao, L., and Seed, L. (2013). A survey on fall detection: Principles and approaches. *Neurocomputing 100*, 144–152.
9. STMicroelectronics. (2011). LIS2DH ultra Low Power Accelerometer Datasheet [online] [accessed 8 September 2015]. Available athttp://www.st.com/web/en/resource/technical/document/datasheet/DM00042751.pdf.
10. Atmel. (2014). ATxmega32C4 Microcontroller Datasheet [online] [accessed 8 September 2015]. Available athttp://www.atmel.com/images/Atmel-8493-8-and-32-bit-AVR-XMEGA-Microcontrollers-ATxmega16C4-ATxmega32C4_Datasheet.pdf.
11. Nordic Semiconductor. (2007). nRF24L01+ 2.4GHz RF Module Product Specification [online] [accessed 8 September 2015]. Available at: http://www.nordicsemi.com/eng/nordic/download_resource/8041/1/88084864.
12. MAXIM Integrated. (2013). MAX1724 Step-up Converter Datasheet [online] [accessed 8 September 2015]. Available at http://datasheets.maximintegrated.com/en/ds/MAX1722-MAX1724.pdf.
13. Korats, G., Hofmanis, J., Skorodumovs, A., and Avots, E. (2015). Fall detection algorithm in energy efficient multistate sensor system. In: *Proceedings of the 37th Annual International Conference of the IEEE Engineering in Medicine and Biology Society, EMBS*.
14. VARTA. (2004). Industrial Alkaline AA Cell Datasheet [online] [accessed 8 September 2015]. Available at http://www.farnell.com/datasheets/627912.pdf.

ENERGOEFEKTĪVAS KRITIENA NOTEIKŠANAS IERĪCES APARATŪRAS IZSTRĀDE

A. Skorodumovs, E. Avots, J. Hofmanis, G. Korāts

K o p s a v i l k u m s

Kritiena laikā vecāka gadu gājuma cilvēkiem ir liela iespēja gūt nopietnu traumu. Šādā gadījumā ir svarīgi laicīgi izsaukt palīdzību, bet vienmēr pastāv iespēja, ka cilvēks atradīsies bezsamaņā un pats to izdarīt nespēs. Šim nolūkam pielieto kritiena detektēšanas sensorus, kuri automātiski informē par kritiena notikumu radiniekus vai sociālo pakalpojumu sniedzējus. Šādas sensora ierīces izstrādes galvenie kritēriji ir algoritma drošība un jaudas patēriņš. Par otras kārtas kritērijiem var uzskatīt ierīces izmēru, svaru un cenu. Šajā rakstā mēs apskatam algoritma darbības principu, argumentējam komponenšu izvēli, pieņemtos lēmumus, apskatam aparatūras un programmnodrošinājuma patēriņa minimizēšanas iespējas, piedāvājam uzmanībai veiktos mērījumus. Balstoties uz testu sērijā iegūtajiem algoritma aktivācijas rezultātiem un izmērīto ierīces patēriņu aktīvajā un gulēšanas režīmā, mēs veicam teorētiskā patēriņa aprēķinus un prognozējām baterijas dzīves ilgumu.

21.09.2015.

LATVIAN JOURNAL OF PHYSICS AND TECHNICAL SCIENCES
2016, N 2

DOI: 10.1515/lpts-2016-0015

RADIO ASTRONOMY

THE INFLUENCE OF WIND TURBINES ON RADIO ASTRONOMICAL OBSERVATIONS IN IRBENE

D. Bezrukovs

Ventspils International Radio Astronomy Centre
101 Inzenieru Str., Ventspils, LV-3601, LATVIA
dmitrijs.bezrukovs@venta.lv

The reflection and diffraction of external communication and navigational transmitters from tall constructions and moving blades of wind turbines produce some short-pulse additional electromagnetic interference strong enough to fully disturb radio astronomical observations. The problem of short-pulse electromagnetic interference is distinctive to all radio telescopes surrounded by wind turbines. This problem became significant for Ventspils International Radio Astronomy Centre (VIRAC) after new wind park "Platene" of Winergy Ltd. was built in 2012 and radio telescopes RT-16 and RT-32 renovated and equipped with cryogenic high sensitive receivers. The paper deals with the analysis and evaluation of intensities and probabilities of short-pulse interferences produced by wind park "Platene" and its possible impact on radio astronomical observations at VIRAC radio telescopes.

Keywords*: electromagnetic interferences, radio astronomy.*

1. INTRODUCTION

Obviously the utilisation of wind power for electricity generation is the growing issue for power generation with a minimal environmental impact. Due to external pressure of "green" organisations, the common EU policy and EU regulations, commercial structures and others, a number of wind power installations are increasing dramatically everywhere. Sometimes the real impact of new wind installations on the local environment appears to be rather unpredictable.

One of wind energy installation effects on a local environment is a possible influence on radio astronomical observations performed by closely located radio telescopes. Tall towers and blades of wind turbines located in the close zones of big radio telescope antennas disturb the uniformity of the electromagnetic environment and produce some additive passive electromagnetic interference. Due to the reflection and scattering of the emission of close communication and navigation transmitters from wind turbine moving blades, periodical shot-pulse interference occurs. This sporadic short-pulse interference is able to fully disturb radio astronomy obser-

vations performed by modern sensitive cryogenic receivers of radio telescopes. The problem mentioned is characteristic of most radio telescopes [2]–[6].

The interference produced by a number of reflected and diffracted side beams has a form of periodical sequences of short pulses with different lengths of milliseconds. In most cases, the interference is sporadic and unpredictable. This kind of interference has a wide and irregular spectrum. The detection and mitigation of similar interference are the most sophisticated task compared to the mitigation of permanent interference by known methods. Taking into account the significance of VLBI (Very Long Base Interferometry) observations, rather weak pulse interference at one of radio telescopes is able to fully violate the observation of the whole radio telescope network.

Along with the creation of wind park "Platene", the problem of pulse electromagnetic interference produced by moving blades of its wind turbines became significant and urgent to radio telescopes RT-32 and RT-16 of Ventspils International Radio Astronomy Centre (VIRAC). The present research is just the first attempt to analyse and evaluate some possible effects of wind park "Platene" on the quality of radio astronomical observations implemented by VIRAC RT-32 and RT-16.

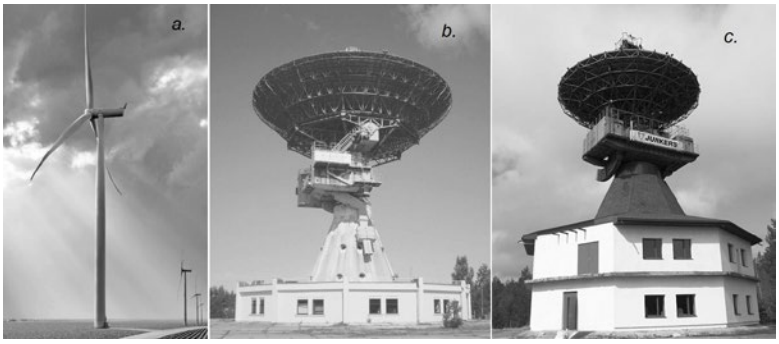

Fig. 1. Siemens SWT-2.3-101 wind turbine, (a) VIRAC radio telescopes RT-32 (b) and RT-16 (c).

2. THE ELECTROMAGNETIC ENVIRONMENT OF VIRAC RADIO TELESCOPES

Radio telescopes RT-16 and RT-32 (Fig. 1, b, c) are the main instruments of VIRAC. After considerable renovation in 2015, they are expected to be involved in a lot of observational programs. The earliest forms are VLBI (Very Large Base Interferometry) in EVN (European VLBI Network), interferometric radio location of space debris and satellites, solar spectral polarimetric observations. Radio telescopes are expected to be equipped with cryogenic radiometers for extended C-band (5 GHz), frequency bands of 327 MHz, 1.8 GHz, 6.3–9.3 GHz are also expected to be used.

Although radio telescopes are located in rather unpopulated site Irbene, they are actually surrounded by a number of various transmitters. Among them several GSM basic stations and digital television transmitters are directly visible and known. A number of maritime and border guard communication, navigation and radio location transmitters are also located in Ventspils and along the sea cost.

In 2012 the wind park "Platene" of Winergy Ltd. was built and started to work permanently. The wind park consists of 13 wind turbines located near Platene (two groups of 4 and 5 wind turbines) and Vede (the group of four wind turbines). The wind park is equipped with widely used SIEMENS SWT-2.3-101 wind turbines (Fig. 1, a). The distance from Irbene radio telescopes to Platene is 19.7 km and to Vede is 8.2 km. Towers of wind turbines are about 100 m in height and turbine blade length is 39 m. Thus, towers and turbines are in the direct visibility from focal centres of both radio telescope antennas above the surrounded forest. Obviously all wind turbines are located in the close zone of at least RT-32 antenna. The mutual location of GSM and digital television transmitters, groups of wind turbines and radio telescopes are shown in Fig. 2.

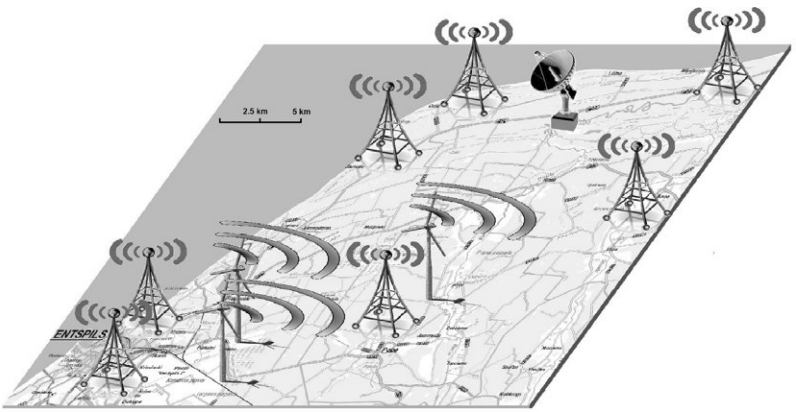

Fig. 2. The location of GSM/DTV towers, groups of wind turbines and VIRAC radio telescopes.

The monitoring of radio interference in Irbene has shown that there is main permanent interference at frequencies of digital television (DVB-T) and GMS mobile communication 900/1800 Mhz. The example of interference monitoring performed in 2014 is shown in Fig. 3. The interference intensity of all GSM transmitters is above the threshold level defined by recommendation [8] and strong enough to produce harmonic interferences in protected radio astronomical frequency bands and intermodulation distortions in the sensitive receiver and frequency conversion units.

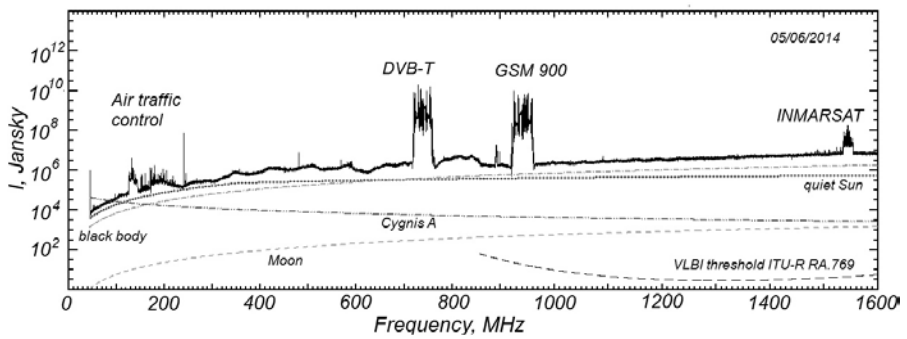

Fig. 3. The spectrum of the isotropic interference flux density in Jansky (1 Ja= 10^{-26} $Wm^{-2}Hz^{-1}$) measured at the secondary focus of RT-32 and its comparison with known radio astronomical sources and threshold limit by recommendation [7].

Radio interference in C-band and higher frequencies is sporadic and the source of it usually cannot be detected precisely. The example of similar sporadic short-pulse interference recorded during the spectral polarimetric observation of the Sun by RT-32 radio telescope is presented in Fig. 4. The interference of 9.3 GHz has a rather narrow frequency band (about 80 MHz – one channel of the 16 band spectral polarimeter for 6.3–9.3 GHz band). The intensity of pulses achieved the spectral flux density of quiet Sun. The source of interference was not detected. During this observation, the antenna azimuth of RT-32 was about 200 deg., so most likely one could explain it as reflection of some maritime radar from towers of "Platene" wind park.

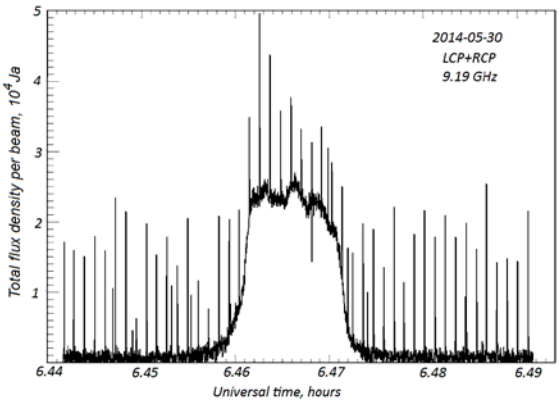

Fig. 4. The record of one Sun scanning by RT-32 during the spectral polarimetric solar observation affected by periodical pulse interference at 9.19 GHz.

3. THE EVALUATION OF PROBABLE PULSE INTERFERENCE PRODUCED BY WIND TURBINES

The precise estimation and prediction of pulse interference produced by wind turbines is a rather sophisticated task. The intensity, pulse time sequence and pulse width depend on the mutual orientation of the wind turbine and radio telescope antenna, receiving equipment and conditions of observations, speed of wind turbine rotation, activity of the transmitter reflected from the wind turbine blade and a lot of other circumstances.

The analysis of possible interference from wind turbines for different radio telescopes involves mostly the evaluation of pulse interference intensity produced by the reflection or scattering of some known or hypotetical transmitter emission and its comparison with the interference threshold limit that could fully disturb the radio astronomical observation [1], [2]. Usually the effective path loss from the transmitter to the radio telescope is obtained taking into account the emission scattering on the wind turbine blade and far side lobes of the antenna pattern diagram [4], [5].

The same evaluation of pulse interference intensities and their appearance probabilities were performed for VIRAC radio telescopes RT-32 and RT16. In this evaluation, hypotetical transmitters of 1 KW power and 100 MHz band width (similar GSM basic station transmitters) located in Ventspils, Jaunupe, Miķeļtornis, Jaunpope, Dundaga are considered.

The interference emission is assumed to be reflected or diffracted from one blade of wind turbines located in Platene and Vede. The radio telescope RT-32 antenna pattern diagram for far side lobes was assumed in recommendation [7] (Fig. 5, a). The spatial passive pattern diagram for the wind turbine blade was assumed similar to the one described in [4]. The diagram consists of the direct reflection from the elliptical cylinder surface and diffraction diagram on the blade edge where the blade is illuminated normally to its surface (Fig. 5, b).

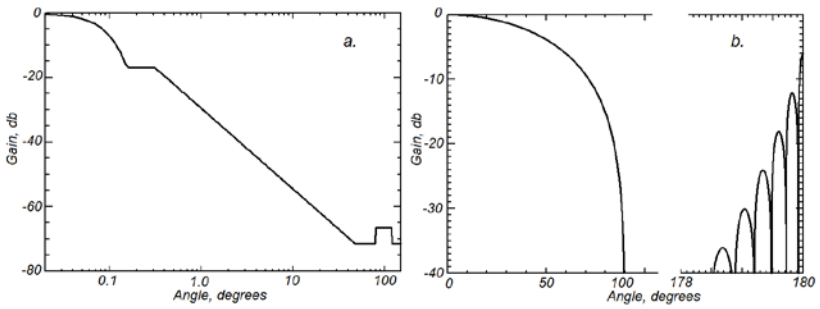

Fig. 5. RT-32 antenna pattern diagram of far side lobes assumed in recommendation [8] (a) and the passive blade reflection and diffraction pattern diagram at 6 cm wavelength (b).

Obviously, the maximal intensity of the pulse interference ("the worst case") can be observed when the radio telescope is directed to the wind turbine (the observational azimuth of RT-32 is 212 deg. to Platene and 188 deg. to Vede) and the antenna elevation is lowest (8 deg. for RT-32). On the other hand, the wind turbine has to be directed to get some maximal reflection of the external transmitter for "the worst case". As a result, calculations under the above-mentioned conditions of spectral flux densities of pulse interference produced by one blade of the wind turbine from some transmitters are shown in Table 1. Spectral flux densities of pulse interference are calculated in Jansky (1 Ja = 10^{-26} $Wm^{-2}Hz^{-1}$) for comfortable comparison with real radio astronomical observation data.

According to recommendation [7], the threshold spectral flux density of interference for C-band VLBI observations does not exceed 100 Ja. Spectral flux densities of radio astronomical sources observed during VLBI session are mostly about 5–50 Ja. Taking into account that the system temperature of new cryogenic receiver is about 20 K, the spectral flux density of some external emission in C-band corresponding to this value is about 30 Ja. Thus, it is evident that in the "worst case" intensities of pulse interference affected by RT-32 do not exceed the threshold level but can exceed intensities of most radio sources in C-band and the system noise of the receiver.

Obviously, the "worst case" of observations is very rare and real intensities of pulse interference should be lower or absent in most cases. The appearance probability of interference related to the "worst case" is shown in Fig. 6. Obtaining the probability of pulse interference appearance, the omnidirectional orientation of wind turbines and prior radio astronomical observations in the southern hemisphere in the range of elevations of about 8–80 degrees was considered. One can evaluate that the

"worst case" is almost impossible, but interference with 10 percent of "worst case" intensity could appear at every fifth observation.

Table 1

The Spectral Flux Density of Maximal Pulse Interference ("worst case") Produced by the Reflection and Scattering of 1 KW Transmitter Emission from the One Blade of a Wind Turbine and Applied to Radio Telescope RT-32 Input

Source	Reflection from Platene	Reflection from Vede
Ventspils	6.9 Ja	5.9 Ja
Jaunupe	8.3 Ja	5.5 Ja
Mikeltornis	2.2 Ja	39.6 Ja
Jaunpope	14.1 Ja	10.4 Ja
Dundaga	0.9 Ja	6.5 Ja

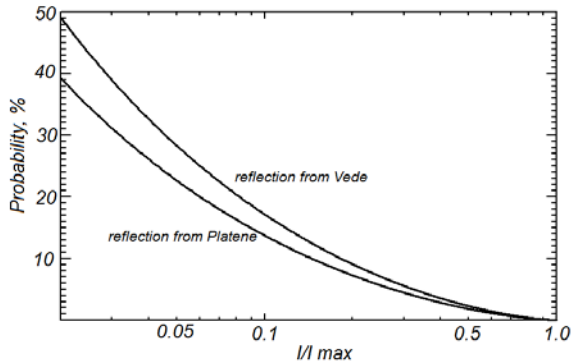

Fig. 6. The dependence of pulse interference probability appearance on the interference intensity related to maximal intensity ("worst case").

Summarising all these issues and taking into account the number of transmitters and wind turbines acting simultaneously, one can conclude that pulse interference produced by wind turbines of wind park "Platene" can actually disturb radio astronomical observations in Irbene.

4. CONCLUSIONS

Even some preliminary and rough analyses and evaluations of intensities of pulse electromagnetic interference produced by towers and moving blades of wind turbines have shown that wind park "Platene" in some cases is able fully to disturb radio astronomical observations performed by VIRAC radio telescopes RT-32 and RT-16. Almost in all other cases the influence of the wind park on observations is still noticeable.

More precise analysis of circumstances of the pulse interference emergence and propagation in the area of Irbene is necessary. The permanent monitoring of electromagnetic interference and determination of its sources must be a mandatory part of the observational activity. Methods of the precise detection of pulse interference appearance and its mitigation have to be developed.

ACKNOWLEDGEMENTS

The present research has been performed in the framework of ESF project "Assessment of Wind Energy Potential in Latvia and Environmental Impact from Wind Energy Installations", 2014/0010/1DP/1.1.1.2.0/13/APIA/VIAA/033.

REFERENCES

1. Jessner, A. (2011). Report on Windfarms and Radio Astronomy. Available at http://www.craf.eu/CRAF-11-01.pdf .
2. Jessner, A. (2010). Wind Power and Radio Astronomy. Available at http://www.craf.eu/windturb/Wind%20Power%20and%20Radio%20Astronomy.ppt.
3. Mattsson, S. (2010). Windturbines vs Radiosystems. Available at http://www.craf.eu/windturb/Vindkraft_Chalmers-Onsala_100427.ppt.
4. Bendz, E. (2010). Electromagnetic Interference from Wind Turbines on Onsala Space Observatory. Available at http://www.craf.eu/windturb/Electromagnetic%20Interference%20from%20Wind%20Turbines%20on%20Onsala%20Space_1.pptx .
5. Bolli, P. (2010). Measurements of Primary Radiation at a Wind Farm Close to the Sardinia Radio Telescope. Available at http://www.craf.eu/windturb/Bolli.ppt.
6. Grypstra, K. (2010). Secondary RF-Emissions from Wind Energy Parks, http://www.craf.eu/windturb/Secondary%20RF-Emissions%20from%20Wind%20Energy%20Parks%20100427.ppt.
7. Recommendation ITU-R RA.769-2. (2003). Protection Criteria Used for Radio Astronomical Measurement. Available at http://www.itu.int/rec/R-REC-RA.769-2-200305-I .
8. Recommendation ITU-R SA.509-1. (2013). Space Research Earth Station and Radio Astronomy Reference Antenna Radiation Pattern for Use in Interference Calculations. Available at https://www.itu.int/rec/R-REC-SA.509-3-201312-I/en.

VĒJA ĢENERATORU IETEKME UZ RADIOASTRONOMISKIEM NOVĒROJUMIEM IRBENĒ

D. Bezrukovs

K o p s a v i l k u m s

Komunikācijas un navigācijas iekāru raidītāju starojums, atstarojoties vai difraģējot no vēja ģeneratora, kas novietots noteiktā augstumā virs Zemes, un no vēja turbīnas kustībā esošām lāpstiņām, rada īsus papildus elektromagnētiskos traucējumus, kas nopietni var ietekmēt radioastronomiskos novērojumus. Pašlaik tāda problēma ir Ventspils Starptautiskā Radioastromonijas Centra (VIRAC) radioteleskopiem, jo vēja parks "Platene" atrodas radioteleskopu antenas tuvajā zonā. Rakstā veikti šādu īsu impulsu traucējumu intensitātes un to parādīšanās varbūtības novērtējumi un to ietekme uz radioastronomiskiem novērojumiem ar VIRAC radio teleskopu RT-16 un RT-32

16.09.2015.

INSTRUCTIONS FOR AUTHORS

"Latvian Journal of Physics and Technical Sciences" ("Latvijas Fizikas un Tehnisko Zinātņu Žurnāls") publishes experimental and theoretical papers containing results not published previously and review articles. Its scope includes: 1) Energy and Power , 2) Physical Sciences, 3) Physics and Applied Physics in Engineering, 4) Environmental Physics and Biotechnology.

Each paper submitted to Journal is evaluated by referees, and is published if the reference is positive.

The review process for papers is Blind Peer Review. The journal does not have article processing charges (APCs) nor article submission charges.

Papers should normally occupy 8 (not more than 10) printed pages including figures (not more than 7), tables, and references.

The title page should contain the title, name(s) of author(s) and address(es) of establishment(s) where the work was carried out.

Form. A paper can be submitted in the electronic (CD or e-mail) form, with indication of the name and address of author with whom the editor will communicate. The paper should be prepared with the text editor WORD for Windows.

Text of the paper should normally be organized as follows: Abstract (the word "Abstract" is not written) with key words (optional); Introduction; Experimental (or Theory); Results, Discussion (or Results and Discussion); Conclusion(s), and References. A summary in Latvian should follow.

Abstract should state briefly the reason for the work and the main results and conclusions. No references, mathematical expressions *etc*. should be included.

Introduction should state the object of the work, its scope, methods and the main advances reported, with brief references to relevant results of other workers.

For papers written in English, the British (UK) version of spelling is preferred; occasionally, US spelling is accepted, provided consistency is observed throughout the text. The use of a computer spell-checker is recommended obligatory.

Format. The following page formatting requirements should be observed:
Paper size A4,

Page setup:	Margins
Top	1.93 cm
Bottom	6.1 cm
Left	5.08 cm
Right	2.92 cm
Gutter	0 cm
From edge	
Header	1.25 cm
Footer	5.33 cm

Font. Times New Roman is preferred, with the 11-point letter size.

Indentions. For the abstract (at the beginning of a text) – 1cm from both sides of the main text; for the 1st paragraph of the text – 1cm from the left; between the lines – single interval, with 2 points below each paragraph. For formulae – 1 cm from the left, 8–10 points from above and below.

Other sizes for formulae according to MathType 6.0 Equation

Size	
Full	11 pt
Subscript/Superscript	8 pt
Sub-Subscript/Superscript	6 pt
Symbol	11 pt
Sub-symbol	8 pt

Figures should be computer-composed.

Tables should be numbered in a sequence corresponding to the order of citation in the text and a short heading should accompany each table.

References in the text should be given as numbers in square brackets and listed in numerical order at the end of the typescript. Examples of published reference are as follows.

Format (APA Style)

Article:

Author(s). (Year of publication). Article title. *Journal Title. Volume* (issue), range of pages.

E.g.: Plumbridge, W.J. (2003). The analysis of creep data for solder alloys. *Soldering& Surface Mount Technology. 15* (1), 26–30. DOI:*

Pauley, M.A., Guan, H.W., & Wang, C.H. (1996). Poling dynamics and investigation into the behaviour of trapped charge in poled polymer films for nonlinear optical applications. *J. Chem. Phys*. *104* (17) 6834–6842, DOI:*

* if available

Book:

Author. (Year of publication). *Book title*. Place of publication: Publisher.

E.g.: Halang, W. (2006). *Integration of fuzzy logic and chaos theory.* Berlin: Springer.

Proceedings from a conference:

Author(s). (Year of publication). Title. In Conference name, Date (Page range). Place of publication: Publisher.

E.g.: Bauer, G.E. (1992). Optics of excitons in confined systems. In Inst. Phys. Conf*.,* 12–14 October 1992 (pp. 45–50). Bristol, UK: Bristol Institute of Physics.

Detailed recommendations are found in www.gruyter.com (*How to enhance reference linking).*

The papers should be sent to the address:
"Latvian Journal of Physics and Technical Sciences"
Institute of Physical Energetics
Aizkraukles iela 21, Rīga, LV-1006, LATVIA
Tel. 67551732, 67558694
e-mail: ezerniec@edi.lv